Politecnico di Milano

SCUOLA DI INGEGNERIA INDUSTRIALE E DELL'INFORMAZIONE
Corso di Laurea Magistrale in Materials Engineering and Nanotechnology

Hybrid perovskite-based solar cells:
photoactive layer morphology optimization towards printed devices.

Candidata:
Giulia SALA
Matr. 820378

Relatore:
Dott. Guglielmo LANZANI

Correlatore:
Dott. Mario CAIRONI

Anno Accademico 2014–2015

A Tony

Contents

Sommario……**vii**

Abstract……**ix**

Introduction……**xii**

1. **Background**……**1**
   - 1.1 Definition and description of solar radiation…… 1
   - 1.2 Photophysics of a solar cell……3
   - 1.3 Parameters of a solar cell……5
2. **Hybrid Perovskites**…… **9**
   - 2.1 Structure and chemical composition……..9
   - 2.2 Bandgap……...11
   - 2.3 Hysteresis…… 14
   - 2.4 Hybrid perovskite solar cell structure…….…….. 17
   - 2.5 Photovoltaic properties of perovskites…… 19
     - 2.5.1 Absorption……...19
     - 2.5.2 Charge carrier transport mechanism in hybrid perovskites……..19
     - 2.5.3 Charge transport mechanism in inverted perovskite solar cells……..21
   - 2.6 Materials and device stability……22
   - 2.7 Deposition methods……23
     - 2.7.1 One step deposition…….. 23
     - 2.7.2 Two steps deposition…… 24
     - 2.7.3 Other methods……24
   - 2.8 Toward large scale Roll-to-Roll production…… 25
   - 2.9 Barcoating……27
3. **Materials and methods**……..**29**
   - 3.1 Materials……29
     - 3.1.1 Hybrid perovskite layer…… 30
     - 3.1.2 Hole Transport Material (HTL)……30
     - 3.1.3 Electron Transport Material (ETL)…….… 31

3.1.4 N-type interlayer……32
3.1.5 Electrodes……32
3.2 Methods……33
3.2.1 Solution preparation……33
3.2.2 Substrate preparation……34
3.2.3 Layer deposition……35
3.3 Characterization……42
3.3.1 J-V under illumination……42
3.3.2 Layers thickness……42
3.3.3 Surface morphology……43
3.3.4 Crystallinity……43
4. Hybrid perovskite morphology optimization……45
4.1 Lead Iodide (PbI_2)……46
4.1.1 Spincoating method……46
4.1.2 Barcoating method……47
4.2 Methylammonium Iodide (MAI)……50
4.2.1 Single step MAI deposition (Dyesol vs. homemade)……50
4.2.2 IPA cleaning……51
4.2.3 Double step MAI deposition……52
4.3 Crystalline structure: XRD spectra……57
5. Devices……62
5.1 Spincoating method……62
5.1.1 Effects of IPA cleaning……63
5.1.2 Effects of consecutive measurements……66
5.1.3 Effects of different double step MAI depositions……66
5.2 Barcoating method……70
5.2.1 Two-step deposition……70
5.2.2 One step-deposition……72

Conclusions……76

Bibliography……78

Ringraziamenti……86

List of figures

0.1 Rate of increasing of power conversion efficiency of perovskite solar cells compared to other types of photovoltaics. From ref. [62]……..... ….ix

1.1 Solar radiation spectrum…… ….2
1.2 Representation of a) ideal cell and b) real cell equivalent models……..6
1.3 I-V characteristic curve of a well performing solar cell. The most important parameters are defined in the picture…… ….6
1.4 Effect of R_s and R_{sh} on the I-V characteristic of a solar cell…… ….8
1.5 Schematics of the shift from the dark characteristic induced by the photogenerated current on the J-V curve under illumination……..….8

2.1 Perovskite crystal structure. From ref. [3]…… ….10
2.2 Calculated *t* and *μ* factors for 12 halide perovskite. From ref. [3]……. ….11
2.3 Perovskite bandgap tuned by the halide composition. From ref. [76].. ….12
2.4 Uv/Vis absorption spectra of $CH_3NH_3PbI_{3-x}Br_3$. From ref. [15]…….. ….14
2.5 I-V curves measured at FS (solid line) and RS (dashed line) for mesostructured devices with a) 220 and b) 110 thick mp-TiO_2 and c) planar device without mp-TiO_2. From ref. [39]……..... ….15
2.6 I-V curves measured at FS and RS for an inverted planar perovskite devices based on PEDOT:PSS/perovskite/PC61BM. From ref. [42].. ….15
2.7 Photocurrents for devices without PCBM layer (orange), with PCBM layers thermally annealed for 15 min (green) and 45 min (blue). Hollows triangles and solid triangles represent the scanning direction from negative to positive bias and from positive to negative bias respectively. From ref. [18]…….….17
2.8 Schematic representation of an inverted planar architectures……..…..18
2.9 Absorption spectra of $CH_3NH_3PbI_3$, $CH_3NH_3PbI_{3-x}Cl_x$ and various semiconductors. From ref. [3]…… ….19
2.10 Photophysical processes and loss mechanisms in perovskite following excitation. From ref. [4]……..21
2.11 (a) Structure of an inverted perovskite solar cell. (b) Scheme of charge transfer dynamics. From ref. [75]……22
2.12 Schematic description of one-step process. From ref. [19]…… ….23

2.13 Schematic description of a two-step process. From ref. [19]…….….24
2.14 Schematic description of a dual-source vapour process. From ref. [25]……..25
2.15 Successive steps in a vapor assisted solution process. From ref. [25]……..….25
2.16 Principles of slot die coating. From ref. [63]……..….26
2.17 Schematic illustration of slot-die coating with a gas quenching process. From ref. [35]…….. ….27
2.18 (a) Structure of wire-bar, (b) schematic diagram of wire-bar coating, and (c) side view of (b). From ref. [61]……..27

3.1 Device structure……..30
3.2 PEDOT (on the left) and PSS (on the right) molecular structure…..……..31
3.3 $PC_{61}BM$ structure……..…….….32
3.4 3.4 AZO structure…….……..32
3.5 The BRAINSON 2510 sonicator used is shown on the left of this figure, while on the right is shown the Diener plasma system…….……34
3.6 Schematic representation of the substrate……..……..35
3.7 Schematics of the four main spin coating steps……..……..35
3.8 Image of the Laurell spin coater used for layer deposition……..36
3.9 TQC barcoater images……..37
3.10 PET positioning on the barcoater, a) side view, b) top view……37
3.11 Schematic representation of the positioning of the different elements: absorbent paper, tape and substrate……..… ….38
3.12 Schematic representation of the positioning of the solution…… ….38
3.13 Schematic representation of the scratched area (on the left) and the active area and the different pixels (on the right)……..…… ….41
3.14 Image (on the left) of the MBRAUN glovebox used for evaporation, annealing and spincoating and (on the right) the appearance of the complete devices…… ….41
3.15 The measurement setup is shown in the picture, with the sample holder positioned under the illumination source and connected to the Keithley 2440 5A source meter…… ….42
3.16 Veeco Decktak 150 profilometer……..…….43

4.1 SEM images of Sample 3…… ….47
4.2 SEM images of a) sample 1 (no gas quenching), b) sample 2 (gas quenching), c) sample 3 at higher magnification……..……..49
4.3 SEM images of a), c) this experiment, b), d) Hwang and co-workers experiment……..……..50
4.4 SEM image of the surface of perovskite layer obtained from a) Dyesol MAI and from b) synthesised MAI……..……..51
4.5 SEM images of a) perovskite layer obtained from a Dysol MAI and b) the same layer after IPA cleaning……..……..52
4.6 SEM images of the samples a)1, b)2, c)3, d)4, e)5, f)6……..…..54
4.7 SEM images of perovskite layers obtained from a)one step Dyesol MAI deposition, b)double step (4+40 mg/ml) dyesol MAI deposition, c)one

step synth. MAI deposition, d) double step (4+40 mg/ml) synth. MAI deposition……..…….55
4.8 SEM images of samples (reported in table 3.3) number a)1 (before IPA cleaning), b)3 (before IPA cleaning), c)4 (before IPA cleaning) and the corresponding after IPA cleaning (d, e, f respectively)……..…..56
4.9 SEM images of a perovskite film with barcoated PbI2 layer a) before and b)after IPA cleaning, respectively……...…….57
4.10 X-ray diffraction spectrum of perovskite thin film obtained from different double step MAI depositions on a spinned PbI2 layer…..……59
4.11 X-ray diffraction spectrum of perovskite thin film obtained from different double step MAI depositions on a barcoated PbI2 layer..…….60
4.12 X-ray diffraction spectrum of perovskite thin film obtained from different double step MAI depositions on a barcoated PbI2 layer…..….61

5.1 Device structure……..63
5.2 J-V Characteristic of a)device 1, b)device 2, c)device 4, d)device 5……65
5.3 Variation of the J-V characteristic of the same device (number 1, first set) due to the increasing number of measurements……..66
5.4 Device structure……..67
5.5 J-V characteristics of a)device 1, b)device 3, c)device 4 and corresponding perovskite morphology (d, e, f, respectively)……..69
5.6 Device structure……..71
5.7 J-V characteristics of devices a)5 and b)6. Below (c), the typical PbI2 morphology printed using the barcoating and the gas quenching techniques……..72
5.8 Device structure……..73
5.9 J-V characteristics of all the devices……..75

List of tables

2.1 Values of energy gap for different iodide perovskites. From ref. [13]…… 13

4.1 Spin parameters, solution concentrations and thickness of different samples……47
4.2 Substrate temperature, solution quantity, quenching parameter and thickness obtained of different samples……48
4.3 MAI type, first step concentration and second step concentration of different samples……53
4.4 Different peaks expected in the XRD spectrum of CH3NH3PbI3 deposited on the top of FTO…….....57

5.1 First set devices parameters……64
5.2 Main parameters (Voc, Jsc, FF and efficiency) obtained from the analysis of figure 5……65
5.3 Second set devices parameters……..…68
5.4 Main parameters (Voc, Jsc, FF and efficiency) obtained from the analysis of figure 5.5…… 70
5.5 Third set device parameters…….....71
5.6 Main parameters (Voc, Jsc, FF and efficiency) obtained from the analysis of figure 5.7…….....72
5.7 Fourth set device parameters…….....74
5.8 Main parameters (Voc, Jsc, FF and efficiency) obtained from the analysis of figure 5.9……..…75

Sommario

Ridurre il consumo di energia, diminuire il consumo di combustibili fossili e abbassare la percentuale di inquinamento, sono considerate le tre principali problematiche al fine di garantire uno sviluppo sostenibile, affiancate dalla ricerca di energie rinnovabili. La luce solare è la principale fonte di energia sulla terra; in una sola ora il sole irraggia la superficie terreste con un'energia pari al consumo globale energetico di un intero anno. Il più grande ostacolo ad uno sfruttamento su ampia scala di questa fonte è la difficoltà nel proporre queste tecnologie ad un prezzo competitivo con quello dei combustibili fossili sul mercato. Negli ultimi cinque decenni, il campo fotovoltaico è stato interessato da un'intensa attività di ricerca, al fine di sviluppare nuove tecnologie che garantiscano buone prestazioni con costi più accessibili. In particolare negli ultimi vent' anni si sono intensificate le ricerche e lo sviluppo di tecnologie a film sottile e/o di terza generazione. Oggi, una buona parte degli sforzi è concentrata sullo sviluppo di dispositivi realizzati attraverso *solution processing*, che abbatte i costi enormi di processo che caratterizzano le tecnologie tradizionali. In particolare, dal 2011 si è assistito al boom nell'interesse e nello sviluppo di una particolare classe di materiali che va sotto il nome di perovskiti ibride. Questi materiali, processabili da soluzioni e che presentano una struttura cristallina con una gabbia inorganica e un catione organico, sono dotati di forte assorbimento ottico, basso tasso di ricombinazione radiativa e facilità di fabbricazione. Dopo il raggiungimento dell'efficienza di 3.9% nel 2011, grazie allo sforzo di molti laboratori nel mondo, l'efficienza ha visto una crescita velocissima, fino a raggiungere circa il 22 % in celle di laboratorio di piccola area. La prossima sfida sarà trasportare il processo di produzione da una scala di laboratorio a una scala di produzione industriale includendo preferibilmente un processo di stampa roll-to-roll con costi competitivi. In questa tesi, la morfologia dello strato fotoattivo di perovskite è stata studiata e migliorata attraverso la tipica tecnica di deposizione su scala di laboratorio: lo spincoating.I risultati ottenuti sono stati poi traslati nella

fabbricazione di dispositivi parzialmente stampati utilizzando la tecnica di stampa di barcoating.

Il lavoro è stato completamente svolto presso il *Center for Nano-Science and Technology@PoliMi (CNST@PoliMi)* dell' *Istituto Italiano di Tecnologia (IIT).*

Abstract

Reduce the energy consumption, decrease the consumption of fossil fuels and lower the percentage of pollution, are considered the three main issues in order to ensure sustainable development, complemented by the search for renewable energy. Sunlight is the main source of energy on earth, in a single hour the sun radiates the earth's surface with an energy equal to the overall energy consumption of a full year. The biggest obstacle to a large-scale exploitation of this source is the difficulty in proposing these technologies at a price competitive with that of fossil fuels on the market. In the last five decades, the photovoltaic field has been interested by an intense research activity, in order to develop new technologies which can guarantee good performance with more accessible cost. Particularly over the last twenty years the research and development of thin film technology and/or third generation have been intensified. Today, a good part of the efforts are focused on developing devices realised through the solution processing, which cut down the huge process costs characterizing the traditional technologies. In particular, since 2011, there has been a boom in the interests and development of a particular class of materials called hybrid perovskites. These materials, solution processable and characterized by a crystalline structure with an inorganic cage and an organic cation, present strong optical absorption, low non radiative recombination rate, together with the ease of fabrication. After achieving the efficiency of 3.9% in 2011, thanks to the effort of many laboratories around the world, the efficiency has seen a rapid growth, reaching about 22% in small area laboratory cells. The next challenge will be translating the lab-scale process to a large-scale production process, which will preferably include a cost-competitive roll-to-roll printing process. In this thesis the perovskite morphology has been studied and improved with the typical laboratory-scale deposition

technique: the spincoating. Then the obtained results were translated in the fabrication of partially printed devices using the barcoating printing technique.

The work has been carried out in the *Center for Nano-Science and Technology@PoliMi (CNST@PoliMi)* of *Istituto Italiano di Tecnologia (IIT).*

Introduction

The past three years have brought large advancements in the area of mixed organic-inorganic halide perovskite materials for solar cells. Perovskite are materials described by the formula ABX_3, where X is an anion and A and B are cations of different sizes. For the organic-inorganic halide perovskite the larger cation B is organic, X is an halogen and B is usually lead. From 2011 until 2014 the maximum power conversion efficiency (PCE) of perovskite-based solar cells has risen from 3.9% [1] to 20.1% [2].

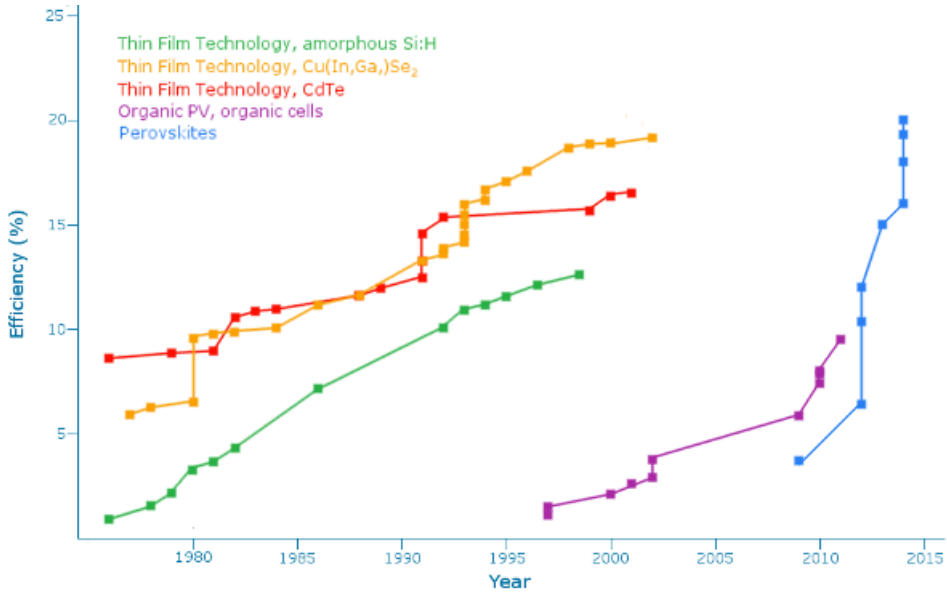

Figure 0.1 Rate of increasing of power conversion efficiency of perovskite solar cells compared to other types of photovoltaics. From ref. [62].

Some key attributes of these perovskites include ease of fabrication, strong solar absorption and relatively low non-radiative carrier recombination rates, considering the simple techniques which are used to prepare them. One negative

aspect is the fact that lead has been a major constituent of all highly performing perovskite cells to date, raising toxicity issues during device fabrication, deployment and disposal. Also, perovskites generally undergo degradation (sometimes quite rapid) on exposure to moisture and ultraviolet radiation [3]. Nevertheless, perovskite solar cells are moreover made from low-cost and earth-abundant materials making them a very promising candidate for future low-cost high-efficiency solar cells [26, 27]. The major development on perovskite solar cells have been reached on small area laboratory scale devices produced using fabrication techniques such as spincoating [78] and physical vapour deposition [79] which are incompatible with low-cost and high-speed mass production. The next challenge will be translating the lab-scale process to a large-scale production process, which will preferably include a cost-competitive roll-to-roll printing process. Up to now there are only few studies that describe the use of scalable solution processes [35, 80]. In one of these all the device's layers are printed using slot-die roll coating and screen-printing in a completely ambient processing. It was found that the scaling resulted in a significant loss in performance. The maximum efficiency achieved was close to 5% [80].
The thesis work here presented has its focus on these issues: the study of the perovskite morphology for improving the quality of the perovskite film formation and crystallization and the implementation of a new perovskite solar cell production method compatible with roll-to-roll processes.

The work has been carried out in the *Center for Nano-Science and Technology@PoliMi (CNST@PoliMi)* of *Istituto Italiano di Tecnologia (IIT)* under the supervision of *Mario Caironi*, Tenure Track Researcher at *CNST@PoliMi* and with the co-supervision of *Carlo Andrea Riccardo Perini*, PhD student at *CNST@PoliMi*.

Chapter 1 gives a description of the solar radiation, the basic photophysics and the most important parameters of a solar cell.
Chapter 2 offers an outlook over organic inorganic halide perovskite: the structure and the chemical composition, along with impact over the optical properties, will be discussed. An overview concerning the most important achievements and the

components of perovskite solar cells is provided, with reference to the physical mechanisms occurring in such devices. Different fabrication techniques are considered.

Chapter 3 explains the choice of the materials used in this work, along with the methods employed for the devices realization and for their characterization.

Chapter 4 reports the optimization of perovskite film morphology for both the processes used (spincoating and barcoating).

Chapter 5 introduces the characterization of three different types of perovskite solar cells processed with two different techniques (spincoating and barcoating).

Chapter 6 summarizes the main achievements of this work of research, drawing the conclusions and suggesting possible future investigations.

Chapter 1

Background

1.1 Definition and description of solar radiation

A photovoltaic cell is a device capable of transforming the electromagnetic energy (photons) into electric energy (charge carriers). This process is defined as primary energy conversion, which is the conversion of different forms of energy into electricity directly without involving intermediate mechanisms. The source of electromagnetic radiation is the Sun, whose behaviour is described by the model of the black body. The spectral emissivity of a black body is equal to:

$$e(v,t)dv = \frac{2\pi v^3 h}{c^3}\frac{1}{e^{\frac{hv}{KbT}}-1}dv \qquad (1.1)$$

where v is the frequency of the electromagnetic radiation, c is the speed of light in vacuum ($2.998*10^8$ m/s), h is the Planck constant ($6.62*10^{-34}$ Js), k_B is the Boltzmann constant ($1.38*10^{-23}$ J/K). The temperature of the surface of the Sun is about equal to 5760 K, therefore the maximum of spectral emissivity is centred approximately at 500 nm, according to the Wien's law:

$$\lambda_{MAX}T = b \qquad (1.2)$$

where λ_{MAX} is the wavelength at which the maximum of emissivity of the black body occurs, T the temperature in Kelvin and b is the Wien constant, equal to

$2.89*10^{-3}$ mK. The major contribution to the Sun emissivity is in the visible range (300 nm – 800 nm), even though a large component is present in the infrared.

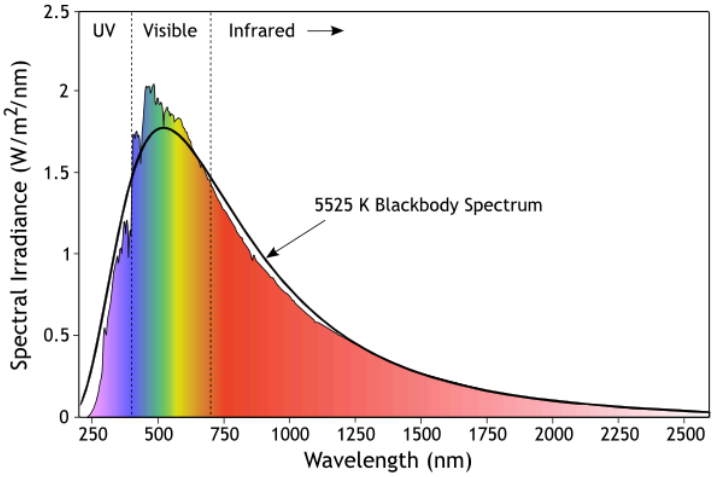

Figure 1.1 Solar radiation spectrum.

Another relevant physical quantity is the spectral irradiance:

$$e(E,T) = \frac{2\pi}{c^2 h^3} \frac{E^3}{e^{\frac{hv}{KbT}} - 1} \tag{1.3}$$

So that *LdE* is the electromagnetic energy emitted per unit surface and unit time with energy between E and E+d. We can define the spectral photon flux b(E,T) as:

$$b(E,T) = \frac{2\pi}{c^2 h^3} \frac{E^2}{e^{\frac{hv}{KbT}} - 1} \tag{1.4}$$

In a similar way, *b*dE is the number of photons emitted by the surface of a black body per unit surface and per unit time with photon energy between E and E+dE. If we integrate the spectral irradiance over all the values of energy, we obtain the energy emitted by the Sun per unit area and unit time, measured on the surface of the Sun, which is equal to 62 MW/m^2. However, the energy conservation principle imposes a reduction in the power density proportional to the inverse of the square power of the distance from the emitting surface. In fact, the spectral photon flux measured outside the Earth atmosphere is equal to:

$$e(E,T) = \frac{2\pi F_S}{c^2 h^3} \frac{E^2}{e^{\frac{hv}{KbT}} - 1} \quad (1.5)$$

F_s is the reduction factor, equal to $\left(\frac{R_{sun}}{d_E}\right)^2$ where R_{Sun} is the Sun radius ($6.96*10^8$ m) and d_E is the Earth distance ($1.496*10^{11}$ m). Integration with respect to energy provides the average incident power per unit of area of the Sun light before it crosses the atmosphere, which is equal to about 1300 W/m2. A further reduction in intensity is expected when the solar radiation moves through air, together with stronger attenuation at specific frequencies, because of scattering and optical absorption. In particular part of the electromagnetic energy converts into vibrational energy of the air molecules, especially in the infrared range since the energy gap between vibrational levels is small. Moreover, the optical path of light varies with the latitude. To account for these variations, an *air mass coefficient* is defined:

$$\eta_{\text{Air Mass}} = \frac{\text{optical path length of light}}{\text{optical path length when Sun is at zenith}} = \frac{1}{\sin\gamma} \quad (1.6)$$

Where γ is the angular height of the Sun over the horizon. When $\gamma = 42°$, which corresponds to temperate latitudes, the air mass factor is equal to 1.5 and the resulting solar spectrum (abbreviated as AM 1.5) is typically used as a reference for the evaluation of the performances of solar cells. It should be noted that the power density associated to the AM 1.5 is 1000 W/m^2 as a conventional standard, while the actual value is around 900 W/m^2.

1.2 Photophysics of a solar cell

The photovoltaic cell working mechanism is based on the interaction between photons and matter. Each photon provides an amount of energy which is equal to $E_{ph} = hv$. In a metal, the Fermi energy represents the highest occupied level, above which only empty states exist. When a photon is absorbed, an electron is

excited to a higher energy level. This configuration is, however, unstable and the electron decays back to the original state, by releasing small quantities of energy as vibrational energy of the crystal by phonon generation. In this way, electromagnetic energy is converted into heat. In a semiconductor, the Fermi energy lies in an energy interval where no electronic states are available, known as bandgap. The bandgap separates two almost continuous sets of energy levels which are called valence band and conductive band. At 0 K and in absence of external stimuli (such as incident light), the valence band is completely filled, while the conductive band is completely empty. When a photon with an energy E_{ph} larger than the bandgap energy E_g is absorbed, an electron is excited from a level in the valence band to another level in the conduction band, leaving an empty state, which behaves as a particle with a positive charge, called hole. The electron and the hole tend to move towards the bottom of the conduction band and towards the top of the valence band, respectively, by releasing energy through collision with phonons. This process is called thermalization or relaxation and it happens in an amount of time of the order of 10^{-15}-10^{-12}s. After a longer period of time the electron will recombine with the hole in the valence band. The recombination occurs with release of a photon with an energy equal to the energy gap and requires from 10^{-9} to 10^{-6}s to happen. Since recombination needs a relatively long time to complete, even 6-7 orders of magnitude longer than the period of time in which recombination takes place, we can extract the charge carriers before the electron recombines with the hole: in this way we obtain electric charges which can do electric work.

In the **Quasi Equilibrium Model** the probability of occupation of a state with energy E by an electron is given by the Fermi Dirac Statistic:

$$f(E) = \frac{1}{e^{\frac{E-\mu}{KbT}}+1} \tag{1.7}$$

Where μ is the chemical potential of the material, which can be replaced by the Fermi energy. The identity between μ and E_F is rigorously true only at T = 0 K, but it is still a good approximation at higher temperature. This probability distribution can be also used to study the population of holes, since the probability of occupation of a state by a hole is equal to the probability of having a missing electron, 1 − f(E). Nevertheless, the Fermi-Dirac statistics provides a

correct description as long as the system is in equilibrium, as for example when the semiconductor is in the dark. As the material is exposed to the electromagnetic radiation, we have absorption of photons and excitation of electrons from the valence band into the conduction band, causing a rise in the number of charge carriers in the two energy bands and pushing the system out of equilibrium. As discussed before, thermalization occurs in a shorter amount of time with respect to recombination. A state of quasi-equilibrium is achieved in the amount of time intervening between relaxation and recombination, where the electron and hole population are in equilibrium with respect to the vibrational energy of the crystal (but not with respect to each other), so that the temperature of the charge carrier populations is equal to the temperature of the crystal. In this case, Fermi Dirac distribution is still valid, but both the electron and hole population are defined by the quasi Fermi energies E_{fn} and E_{fp}. The difference between E_{fn} and E_{fp} is known as chemical potential of radiation ($\Delta\mu$) and is equal to the maximum electrical work which can be done by an electron-hole pair extracted from the solar cell. In particular, the higher the illumination intensity is, the larger the number of photogenerated electron-hole pairs is, giving a larger $\Delta\mu$.

1.3 Parameters of a solar cell

The behaviour of a solar cell is described by the I-V characteristic curve, which relates the current I delivered by the solar cell under a given applied voltage drop V. Since the current is roughly proportional to the illuminated area of the device, we may adopt the current density J as physical quantity for comparison. In order to define the equation related to the characteristic curve, we need to develop the equivalent electrical model. The simplest description is the ideal case, where the solar cell corresponds to an ideal current generator and an asymmetric non-linear resistive element, a diode. In the real case, instead, part of the power is dissipated because of several factors. A non perfect contact between the semiconductor and the metal electrodes yields a voltage drop at the junction. Moreover, leakage currents may occur at the sides of the device or in correspondence to defects, such as pinholes. These two effects are equivalent to

two parasitic resistances which are, respectively, the series resistance R_S and the parallel resistance R_{SH}. The current density equation becomes:

$$J(V) = J_{sc} - J_0\left(e^{\frac{e(V+JAR_S)}{KbT}} - 1\right) - \frac{V+JAR_S}{AR_{SH}} \qquad (1.8)$$

where *A* is the active area of the device. It is possible to see that, if $R_{SH}\rightarrow 1$ and $R_s\rightarrow 0$, we have the equation of the ideal solar cell.

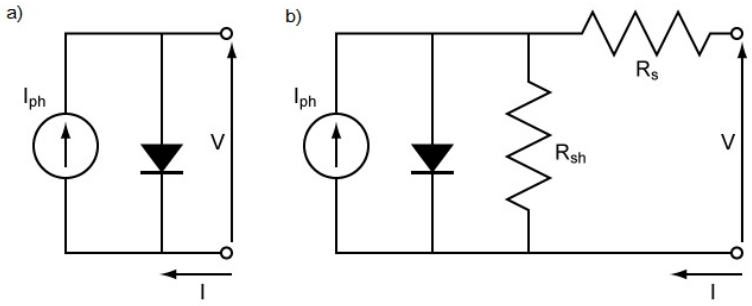

Figure 1.2 Representation of a) ideal cell and b) real cell equivalent models.

Different parameters (fig. 1.2) delineate the behaviour of the solar cell:

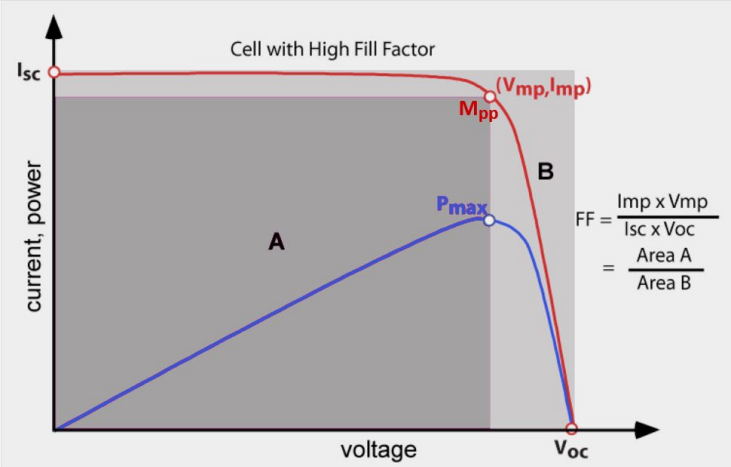

Figure 1.3 I-V characteristic curve of a well performing solar cell. The most important parameters are defined in the picture.

The **short circuit current density J_{SC}** is defined as the value of the current observed when the voltage applied at the terminals of the solar cell is equal to 0. It is the highest value of current a cell can produce and, in the ideal model, it is equal to the photogenerated current. The **open circuit voltage V_{OC}** is the difference in potential which must be applied in order to have no current running through the cell. According to the aforementioned model, it is the value of the

potential at which the dark current and the photocurrent cancel out. The operating regime of a solar cell is the bias interval from 0 to V_{OC}, where the cell can deliver power. The power density is given by :

$$P(V) = J(V)V \tag{1.9}$$

P reaches its highest value when the cell works at the maximum power point, which is identified by the voltage V_M and the current density J_M. The **Fill Factor (FF)** is defined as the ratio:

$$\mathrm{FF} = \frac{J_M V_M}{J_{SC} V_{OC}} \tag{1.10}$$

It denotes how close the actual J-V curve is with respect to the case of an ideal diode, where the current density follows a steplike trend. The efficiency of a solar cell is the ratio between the power density, which is generated by the device at the maximum power point, and the power density of incident radiation:

$$\eta = \frac{P(V)}{P_{inc}} = \frac{FF J_{SC} V_{OC}}{P_{inc}} \tag{1.11}$$

and it can be written as a function of J_{SC}, V_{OC} and FF. This expression allows to determine the impact of different factors (energy gap, thickness, purity, crystallinity, etc.) on these three parameters and, thus, on the overall efficiency of the cell. The series resistance R_S is roughly equal the inverse of the slope of the I-V curve at the V_{OC}, while the parallel resistance R_{SH} is approximated by the inverse of the slope at I_{SC}. The ideal cell model predicts a value of R_S equal to 0 and a value of R_{SH} equal to infinite. As R_S increases and/or R_{SH} decreases, we expect changes in the shape of the I-V curve: an increase in R_S does not affect V_{OC} while I_{SC} drops for high values of resistance. On the other hand, a decrease in R_{SH} leaves I_{SC} unchanged, but V_{OC} falls as low values of resistance are attained (see fig. 1.3).

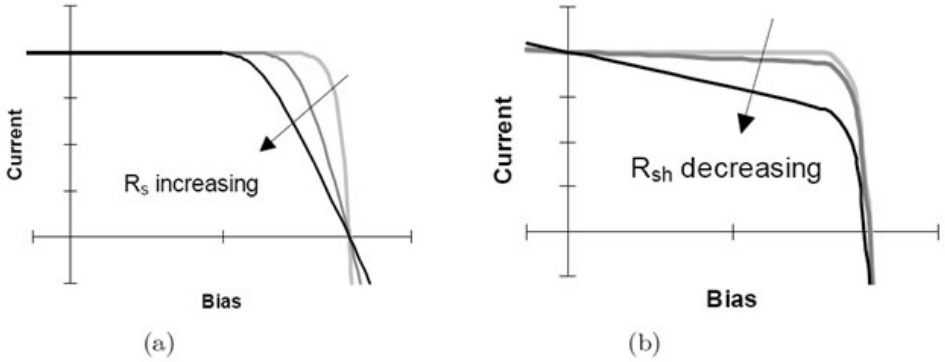

Figure 1.4 Effect of R_s and R_{sh} on the I-V characteristic of a solar cell

In low light conditions the effect given by high R_s is strongly suppressed, while the sensibility to low R_{sh} is increased. From the analysis of the experimental J-V dark characteristic R_s, R_{sh} and η might be inferred.

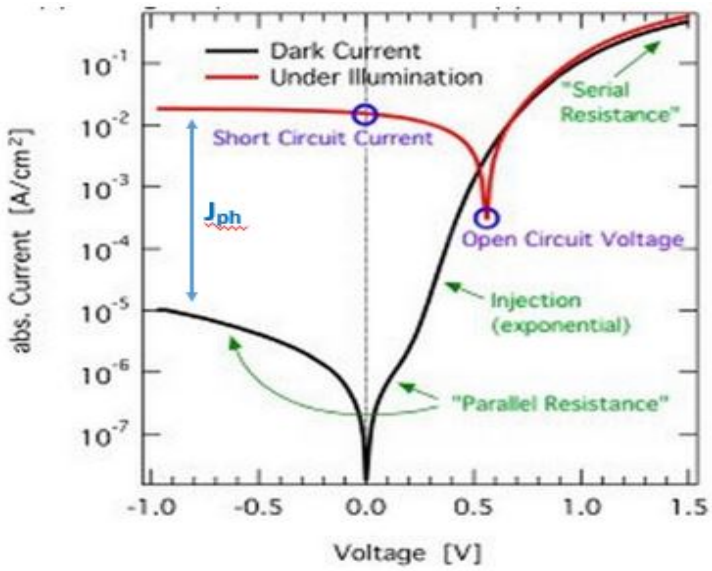

Figure 1.5 Schematics of the shift from the dark characteristic induced by the photogenerated current on the J-V curve under illumination.

Chapter 2

Hybrid Perovskites

Perovskite is the common name for compounds whose composition is defined by the generic chemical formula ABX_3, in which A and B are cationic species with a different size (typically A is larger than B) and X is an anionic species. Organic-inorganic halide perovskites are object of large interest for application in photovoltaic devices because of their attributes, such as ease of fabrication, strong solar absorption and low non-radiative recombination rates. All these features make this material promising for the realization of cheap devices with high energy conversion efficiencies. However there are also significant drawbacks: the use of lead, which is a major constituent of all highly performing perovskite, raises concerns about toxicity during cell fabrication, deployment and disposal, while the rapid degradation, when they are exposed to humidity or ultraviolet radiation, limits the life of complete devices [3].

2.1 Structure and chemical composition

Perovskites usually have a cubic or pseudocubic unit cell, where the cation A is located at the corners of the cube, while the cation B resides at the cell center and it is surrounded by 6 anions X (situated at the face centers) in an octahedral cluster $[BX_6]^{4-}$ [4].

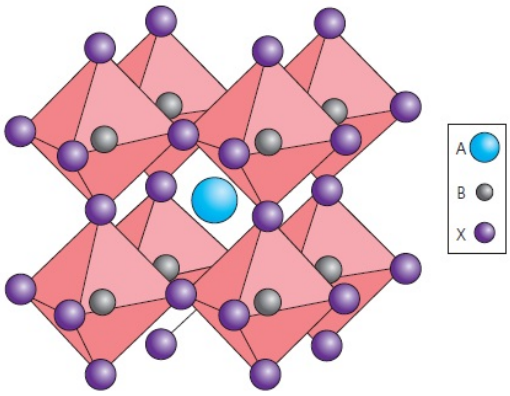

Figure 2.1 Perovskite crystal structure. From ref. [3]

Two important parameters which describe the crystalline structure of perovskites are the tolerance factor *t* and the octahedral factor *μ*. In an idealized solid-sphere model, t is defined as the ratio between distance A-X and distance B-X, while μ is equal to the ratio of the radius of ionic species B to the radius of ionic species X. If we refer to the crystal structure depicted in fig.1.7, t is equal to:

$$t = \frac{R_a + R_b}{\sqrt[2]{2}(R_b + R_x)} \qquad (2.1)$$

where R_a, R_b and R_x are the ionic radii of the respective ionic species. For halide perovskites (where X is a halogen, such as F, Cl, Br, I) the value of t ranges between 0.81 and 1.11 whereas μ varies from 0.44 to 0.90 [5]. We observe that the cubic structured shown in fig.1.7 is likely to occur when the value of t lies in the interval 0.89-1.0. Lower values of t lead to less symmetric tetragonal or orthorhombic habits.

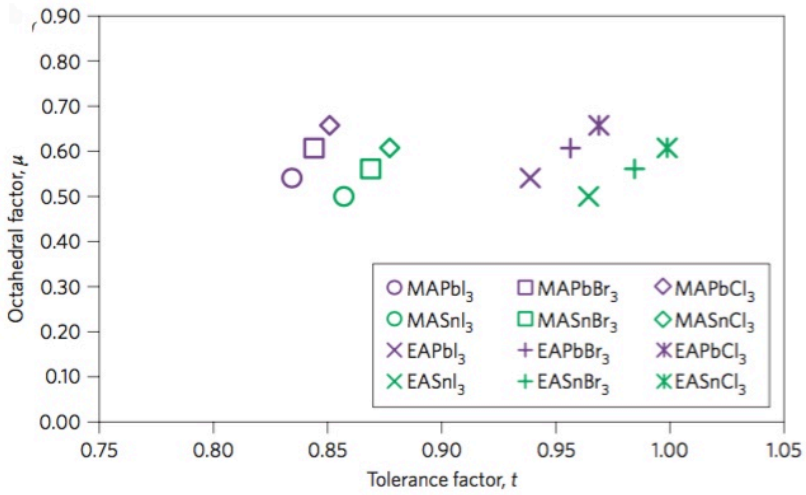

Figure 2.2 Calculated *t* and *μ* factors for 12 halide perovskite. From ref. [3]

Regardless of these constraints, transitions between different phases with temperature are observed for any type of perovskite, where the high-temperature phase is generally cubic.

Organic-inorganic halide perovskites posses a large organic cation A, generally methylammonium ($CH_3NH_3^+$) with R_a = 0.18 nm, even if ethylammonium ($CH_3CH_2NH_3^+$ with R_a = 0.23) and formamidinium ($NH_2CH{=}NH_2^+$, with R_a estimated to be in the range 0.19- 0.22 nm). Anion X is a halogen: Iodine (R_X = 0.22 nm) is the most used one, although Bromine and Chlorine (R_X = 0.196 and 0.181 respectively) are employed, especially in mixed halide perovskites. Lead is used as cation B (R_b = 0,119): some attempts have been tried with other elements (Sn, Eu,…), but always leading to low performances. The standard inorganic-organic halide perovskite is therefore methylammonium lead triiodide ($CH_3NH_3PbI_3$), but mixed halides $CH_3NH_3PbI_{3-x}Cl_x$ and $CH_3NH_3PbI_{3-x}Br_3$ find use as improved features can be exhibited.

2.2 Bandgap

We can easily tune the bandgap of a halide perovskite (ABX_3) by varying the combination of all three components. Band gap tuning is required to extend the absorption to longer wavelength, thus enhancing the light harvesting. The electronic structure of halide perovskite is dominated by the characteristics of the

B-X bond. In a 3D $CH_3NH_3PbI_3$ crystal the valence band maximum consists of the Pb 6p–I5p antibonding orbital, while the conduction band minima comprises Pb 6p–I5s antibonding and Pb 6p–I5pπ antibonding orbitals [6]. The bottom of the conductive band has an energy equal to about -3.93 eV (with respect to the vacuum energy) and the top of the valence band level has an energy equal to about -5.43 eV, with a related energy gap equal to about 1.5 eV.

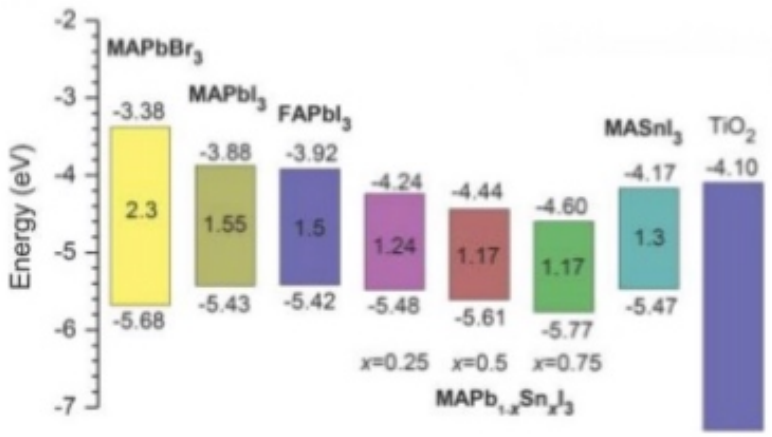

Figure 2.3 Perovskite bandgap tuned by the halide composition. From ref. [76]

The bandgap of perovskites tends to decrease when: (1) the dimensionality of the BX_6 network increases [7], (2) the B-X-B bond angle increases [8], (3) the electronegativity of the anionic species decreases [9], (4) the difference in the electronegativity between the metal cation and the anion decreases [7]. The cation A does not play a major role in determining the band structure, but it can still influence the optical properties by deforming the BX^{6-} octahedron network due to the variation of its size, since a larger or smaller cationic species causes the whole lattice to expand or contract. If we refer to a generic compound $APbI_3$, we see that the value of R_a cannot be larger than 2,6 Å, so to maintain the tolerance factor equal to 1. As the ionic radius of cation A increases, we expect the crystal structure to expand and the bandgap to decrease, leading to a shift towards the red in the absorption onset [10]. This is the reason why $CsPbI_3$ is capable of absorbing up to a shorter wavelength, while $FAPbI_3$ absorbs up to a longer wavelength than $MAPbI_3$, as the trend in the length of ionic radii is $R_{Cs+}<R_{MA}+<R_{FA+}$. As mentioned before, Lead (major metal cation B) is the

primary choice as metal cation B in perovskite for solar cells. In a crystal with composition AMI_3 (where M = Pb, Sn, Ge) , the M-I-M bridging angles in the MI_6 octahedra are 166.27° for Ge, 159.61° for Sn and 155.19° for Pb [8]. At the same time the electronegativity of the metal cation increases as we move up in the group, causing an increase in the covalent character of the M-I bond. For these two reasons, the bandgap follows the trend $AGeI_3$<$ASnI_3$<$APbI_3$. Therefore, Sn(II) based perovskites could be employed in order to improve the efficiency of the solar cells in the near infrared. Apart from these considerations, Tin (Sn) is an appealing alternative to Lead also because it would allow the production of perovkite solar cells embedding a less toxic metal. However, the stability of the oxidation state 2^+ decreases as we move up in the group 14 of the periodic table. Specifically, Tin is not stable in the form Sn^{2+} and it has a tendency to be oxidized to the form Sn^{4+}. This process alters the charge neutrality of the perovskite structure, resulting in the formation of oxides/hydroxides of Tin and methylammonium iodide [11]. Compounds where Pb has been partially substituted by Sn have not shown substantial stability in time either [12].

Material	Energy Gap (eV)
$CH_3NH_3SnI_3$	1.20
$HC(NH_2)SnI_3$	1.41
$CH_3NH_3PbI_3$	1.52
$HC(NH_2)PbI_3$	1.48
$CsSnI_3$	1.30
$CsPbI_3$	1.67

Table 2.1 Values of energy gap for different iodide perovskites. From ref. [13]

Absorption spectra for Pb halide perovskites shift towards longer wavelengths when we move down the group of halogens (from Chlorine to Bromine to Iodine)[14]. The redshift in the bandgap is explained with the increase in the covalent character of the chemical bonding with Lead. A perovskite structure which incorporates two halides such as iodide and bromide [15] or bromide and chloride [16] enables a continuous tuning of the bandgap and the optical absorption, while no evident correlation was found between the composition of iodochloride mixed perovskites and the value of their bandgap.

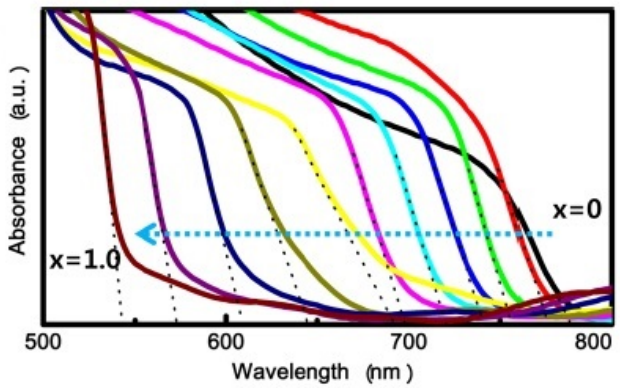

Figure 2.4 Uv/Vis absorption spectra of $CH_3NH_3PbI_{3-x}Br_3$. From ref. [15].

2.3 Hysteresis

All perovskite solar cells exhibit a particular phenomenon, which is known as hysteresis [17]. This expression refers to the strong dependence of the current-voltage characteristic curve on several factors, such as: (1) the scanning direction, whether it is forward scan, from short circuit to open circuit, or reverse scan, the opposite way, (2) the voltage sweep rate, namely the scan rate, (3) operational condition before scanning (open circuit, short circuit, in the dark), (4) incident radiation intensity, (5) structure and components of the device and (6) processing conditions. The origin of hysteresis is still open to debate, although defects and polarizability of the perovskite have been proposed as possible reasons. The use of a mesoporous TiO_2 scaffold significantly impairs the hysteresis effects, while the corresponding planar devices suffer from severe hysteresis (Fig. 2.11) [38, 39, 40, 41].

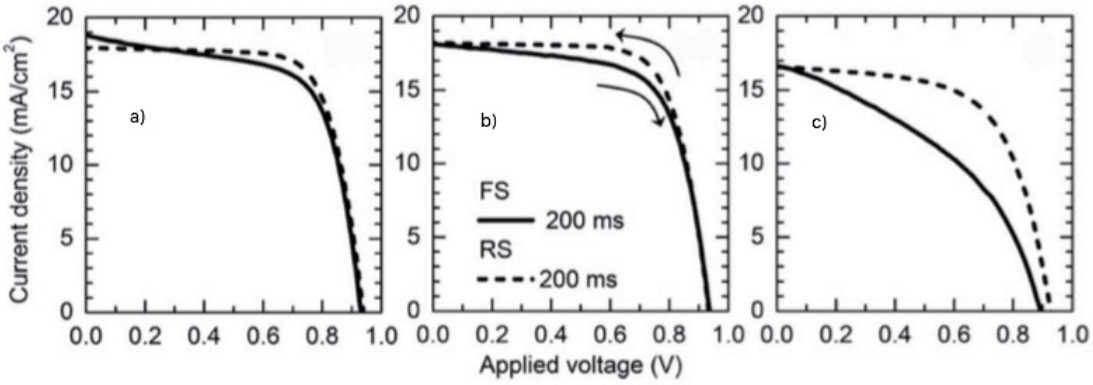

Figure 2.5 I-V curves measured at FS (solid line) and RS (dashed line) for mesostructured devices with a) 220 and b) 110 thick mp-TiO_2 and c) planar device without mp-TiO_2. From ref. [39].

Kim and Park discovered that the low-frequency capacitance was higher in a planar device, suggesting that a planar substrate could induce dipole polarization in $CH_3NH_3PbI_3$ perovskite films, which was considered to be the cause of the hysteresis [39]. On the other hand, Snaith et al. proposed that the severity of hysteresis was dependent on the quality of interface between perovskite and the charge-selective contacts [40]. Due to the higher surface area, charge transfer between perovskite and a mesoporous TiO_2 scaffold is more efficient, resulting in diminished impact of the phenomenon. Interestingly, inverted planar perovskite devices based on PEDOT:PSS/perovskite/$PC_{61}BM$ with high efficiencies have been reported without any observed hysteresis (Fig. 2.12).

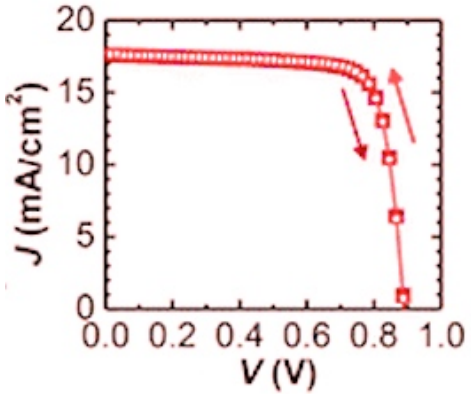

Figure 2.6 I-V curves measured at FS and RS for an inverted planar perovskite devices based on PEDOT:PSS/perovskite/PC61BM. From ref. [42].

We also note that the photoluminescence quenching of $CH_3NH_3PbI_{3-x}Cl_x$ with PEDOT:PSS and $PC_{61}BM$ is more efficient than with spiro-OMeTAD and TiO_2, respectively [48]. This can be translated into a more efficient hole transfer from the perovskite layer to PEDOT:PSS than to spiro-OMeTAD and a more efficient electron transfer from the perovskite layer to $PC_{61}BM$ than to TiO_2.

Perovskite absorbers may have a significant defect density within or near the surface of the material or specifically generated interface states. Such defects can act as traps for electrons and holes and fill under forward bias working conditions, while they may empty due to direct charge transfer to the n- and p-layers, resulting in poor operations until traps are filled once again. If this is the correct interpretation, or the predominant mechanism, lack of hysteresis at very high scan rate is a consequence of emptying the trap sites towards short circuit occurs at a slower rate with respect to the voltage sweep. Trapping and detrapping time may depend on the architecture and processing of the device. Shao and colleagues demonstrated that the use $PC_{61}BM$ can passivate the trap states on the surface and grain boundaries of perovskite films. A layer of PCBM is deposited on the top of perovskite film as a component of a multipart electron-extracting layer in an inverted perovskite solar cell. A thermal annealing is performed at 100°C for 45 minutes in order to favour diffusion of fullerenes along the grain boundaries. The net result of this process is the decrease of the trap density by two orders of magnitude. At the same time, photocurrent hysteresis is almost completely cancelled (see Fig. 2.13) [18].

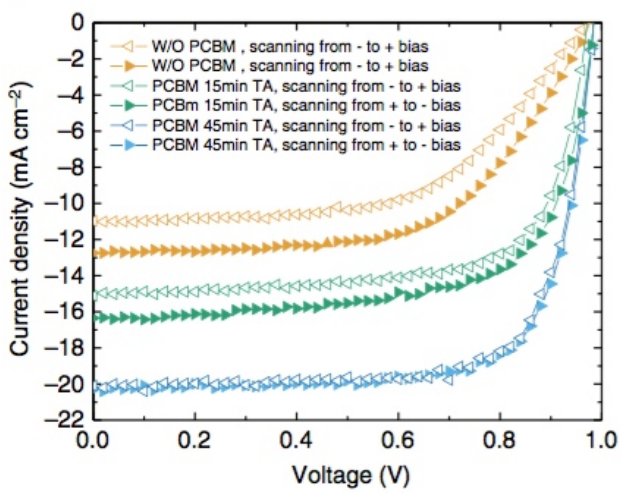

Figure 2.7 Photocurrents for devices without PCBM layer (orange), with PCBM layers thermally annealed for 15 min (green) and 45 min (blue). Hollows triangles and solid triangles represent the scanning direction from negative to positive bias and from positive to negative bias respectively. From ref. [18].

2.4 Hybrid perovskite solar cell structure

The device performance of perovskite solar cells is highly dependent on their architecture which will in turn dictate the choice of materials, the deposition methods for the material and naturally, the compatibility between the different components in the device. Two major embodiments of perovskite solar cells have been developed so far, mesoscopic and planar structures. The planar architecture can exist in either conventional or inverted configuration, depending on the direction of electric current. From now on we will focus only on the inverted planar structures, which is the one that will be used in this thesis work.

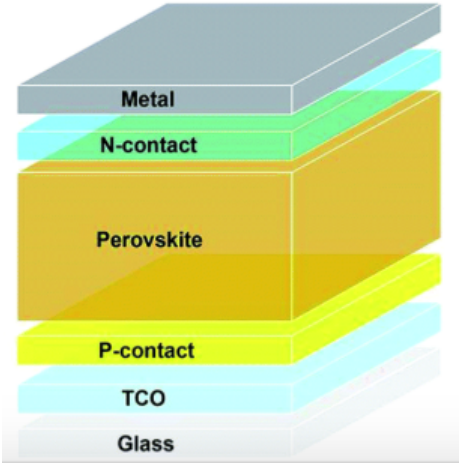

Figure 2.8 Schematic representation of an inverted planar architectures.

The first few papers employing **inverted "p–i–n" architecture** are based on a solution-processable organolead halide perovskite sandwiched between a p-type conducting polymer (PEDOT:PSS) and an n-type fullerene derivative ($PC_{61}BM$), with a PEDOT:PSS layer coated directly on the transparent conductive substrate [36, 37]. Devices with this architecture have also experienced significant performance enhancement in a very short time, from a PCE of mere 3.9% to more than 15%. Some HTMs that have been used in inverted planar-heterojunction perovskite solar cells include PEDOT:PSS, polythiophene, spiro-OMeTAD, graphene oxide (GO), NiO, V_2O_5 and CuSCN. PEDOT:PSS is one of the most commonly used. Charge selectivity of PEDOT:PSS can be further improved by employing a thin layer of poly-arylamine (polyTPD) between PEDOT:PSS and perovskite, forming thus a bilayer HTL [64]. A blend between PEDOT:PSS and perfluorinated ionomer (PFI) yields a higher performance with respect to the reference cell, which is thought to be due to the self-organization of PFI in the blend, causing a better energy level alignment at the interface between the HTL and the perovskite. Inorganic NiOx is a frequently used HTM. High temperature annealing processes (300°C–500°C) can be avoided with low temperature sputtering deposition. Efficiency equal to 15.4% is delivered by an inverted structure perovskite solar cell where the HTM is Copper doped NiOx. Fullerene (C_{60}) and its derivatives are the most widely used n-type materials for ETLs in inverted perovskite solar cells. It has been demonstrated that $PC_{61}BM$,

one of the more commonly used fullerene derivatives, could effectively quench the photoluminescence of $CH_3NH_3PbI_3$, suggesting a high probability of efficient charge transfer [36]. Apart from $PC_{61}BM$, other fullerene compounds have been used in similar device configurations: C_{60}, ICBA and $PC_{71}BM$.

2.5 Photovoltaic properties of perovskites

2.5.1 Absorption

Strong optical absorption is the key to the outstanding performance of these perovskite cells, reducing both the required thickness and the challenges in collecting photogenerated carriers. Absorption measurements (Fig. 1.14) are consistent with calculations showing direct-bandgap properties for perovskites of interest [73, 74].

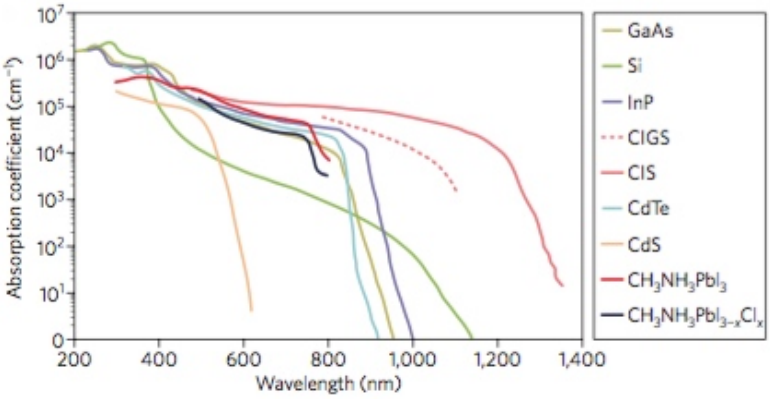

Figure 2.9 Absorption spectra of $CH_3NH_3PbI_3$, $CH_3NH_3PbI_{3-x}Cl_x$ and various semiconductors. From ref. [3].

2.5.2 Charge carrier transport mechanism in hybrid perovskites

Perovskites support ambipolar charge transport: $CH_3NH_3PbI_3$ films obtained from solution processes can achieve really long diffusion lengths: up to 1069 for electrons and 1213 for holes [65]. These charge diffusion lengths are much larger than the typical values observed in solution processed materials (of the order of 10 nm) [66], thermally deposited organic molecules (10 - 50 nm) [67], colloidal quantum dots (30-80 nm) [68]. The effective masses of both electrons and holes

in $CH_3NH_3PbI_3$ are quite small: $m_e^* = 0.23m_o$ and $m_h^* = 0.29m_o$ [69]. The long electron-hole diffusion length is associated with the fact that both the monomolecular and bimolecular charge carrier recombination rates are very low [70]. A monomolecular recombination is a process that involves one free carrier at a time. Trap assisted recombination is one example of this kind of recombination: an electron is trapped in a recombination center and subsequentely recombines with a hole. Bimolecular recombination instead involves two free carriers at a time, such as direct band-to-band recombination, is generally referred to as bimolecular recombination. However a third type of recombination mechanism may occur in which three free carriers are involved simultaneously. An example is a three-body collision in the Auger intrinsic recombination (in which one electron in the conduction band recombines with a hole in the valence band and the energy released is taken up by a third particle-electron). This process is defined as trimolecular recombination or three-body recombination. In perovskites, the Auger recombination (which is a third order mechanism) rate is found to be as high as about 10^{-29} cm^6s^{-1}, while it is two orders of magnitude smaller in highly doped bulk Si wafers [71]. Amplified spontaneous emission out-competes Auger recombination at high photoexcitation densities [72]. Nonetheless, under solar light intensity (low intensity excitation) spontaneous emission is strongly suppressed and, in general, all the non-radiative mechanisms are weak, so organic-inorganic halide perovskites behave as perfect photovoltaic materials.

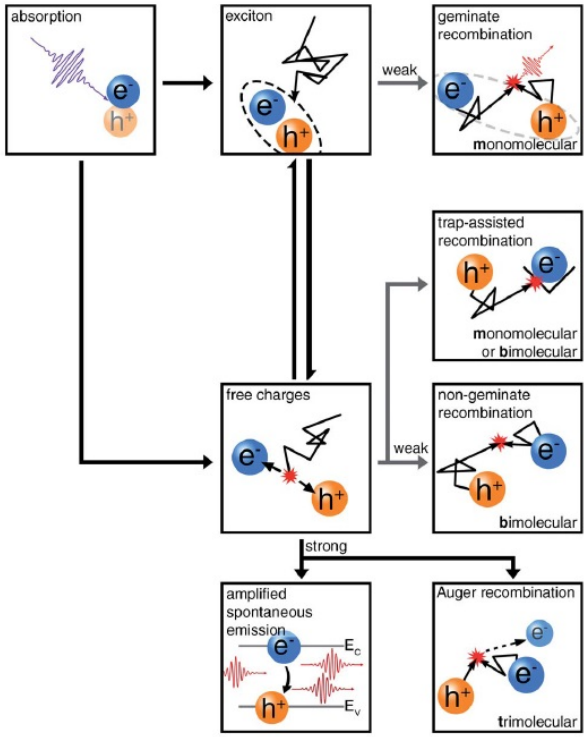

Figure 2.10 Photophysical processes and loss mechanisms in perovskite following excitation. From ref. [4]

2.5.3 Charge transport mechanism in an inverted perovskites solar cells

The inverted $MAPbI_3$ planar perovskite hybrid solar cells (depicted in fig. 2.9a) consists of ITO/PEDOT:PSS/$MAPbI_3$/PCBM/Au. Upon illumination, the holes (electrons) generated in $MAPbI_3$ are efficiently transported to the electrode through the PEDOT:PSS (PCBM) intermediate layer, without significant charge accumulation at traps in the PEDOT:PSS/$MAPbI_3$/PCBM layer because of the similar charge carrier mobility in each layer [75].

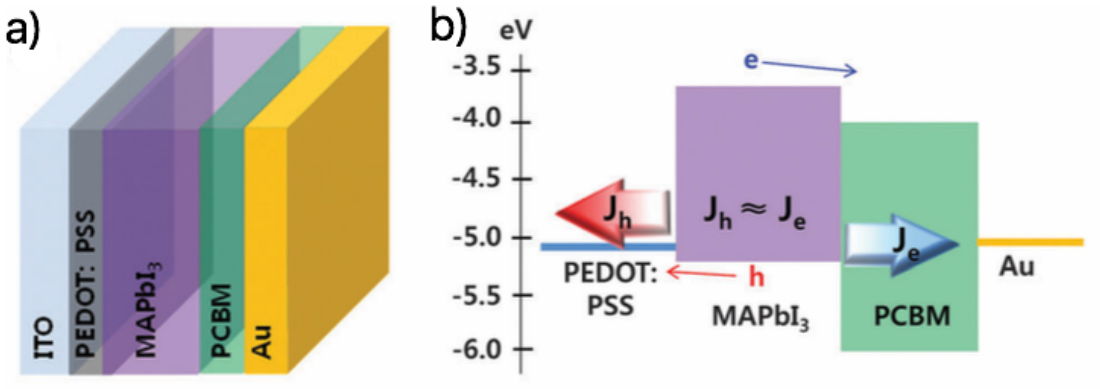

Figure 2.11 (a) Structure of an inverted perovskite solar cell. (b) Scheme of charge transfer dynamics. From ref. [75].

2.6 Materials and device stability

Organometal halide perovskites are intrinsically susceptible to moisture and heat, while the organics in the cells tend to degrade in the presence of moisture, oxygen and heat. The instability of lead halide perovskites (e.g., $CH_3NH_3PbI_3$) in a humid environment is often reflected by the decrease in film absorption between 530 and 800 nm, as reported by Niu et al [43]. The moisture-induced degradation of $CH_3NH_3PbI_3$ is also evident from the disappearance of the XRD peaks related to the initial perovskite structure and the emergence of peaks corresponding to the degradation products comprising PbI_2 and I_2; the formation of I_2 is triggered only when both moisture and light are present. Habisreutinger et al. also pointed out that the colour change from dark brown/black to yellow in lead halide perovskite films upon degradation in air could be attributed to the bond dissociation among the crystal units induced by the interaction between water molecules and the highly hygroscopic methylammonium cations, resulting in the transformation of the perovskite crystal structure to a lower dimensional system [44]. Therefore, perovskite solar cells require stringent encapsulation to ensure a long outdoor operational lifetime.

2.7 Deposition methods

Different techniques have been developed for the deposition of Organometal halide perovskites. All of them are based on the same principle: the combination of an organic component, such as methylammonium iodide (MAI), with an inorganic component, such as PbI_2 or $PbCl_2$, to form the perovskite ($MAPbI_3$ or $MAPbI_{3-x}$ Cl_x, respectively). In the following section the most common deposition methods will be presented, with a focus on solution processable deposition techniques.

2.7.1 One-Step deposition

One-step precursor deposition is the most common thin film deposition method for photovoltaic devices because of its intrinsic simplicity. The precursor solution for perovskite crystal is prepared by mixing powder of MX, where M could be methylammonium or formamidinium cations and X PbI_2 or $PbCl_2$ or $PbBr_2$ at the 1:1 stoichiometric or at 3:1 non-stoichiometric mole ratio. The solvent is a high boiling point aprotic polar species, such as dimethylformamide (DMF), dimethylacetamide (DMAc), Dimethylsulfoxide (DMSO), N-Methyl-2-pyrrolidone (NMP), γ-Hydroxybutyric acid (GBL), etc. The solution is used at elevated temperature in order to have the complete dissolution of the solute in the solvent. The mixture is spin-coated onto a substrate, and the perovskite is formed through an annealing process at around 100°C.

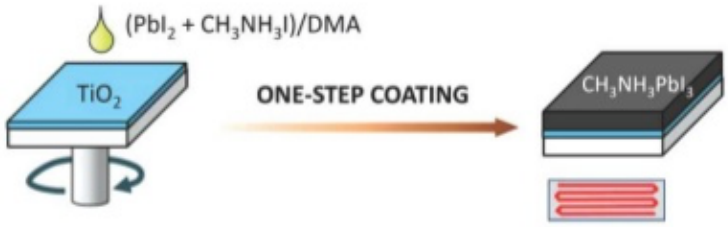

Figure 2.12 Schematic description of one-step process. From ref. [19].

2.7.2 Two-Step deposition

Two-step mechanism was first used by Burschka and co-workers to fabricate a perovskite thin film solar cell [20]. They first spin-coated PbI_2 from solution in DMF onto a mesoporous titanium dioxide film and successively transformed in perovskite ($CH_3NH_3PbI_3$) by dipping into a solution of MAI in isopropanol. The formation of the perovskite crystals is instantaneous and is practically complete after a few seconds of immersion. The driving force for this process is the difference in bulk lattice energy for the two materials (PbI_2 and $CH_3NH_3PbI_3$), where the initial crystal lattice serves as a template for the formation of the final compound. In PbI_2 the insertion of the organic compound is facilitated by the layered structure, which consists of three spatially repeating planes I–Pb–I [21]. The strong intralayer chemical bonding, as well as weak Van Der Waals interactions, assists the insertion of guest molecules between these layers [22]. All these specific features, combined with the nanoscopic morphology of PbI_2 precursor that enhances the reaction kinetics, allows the transformation to take place in few seconds.

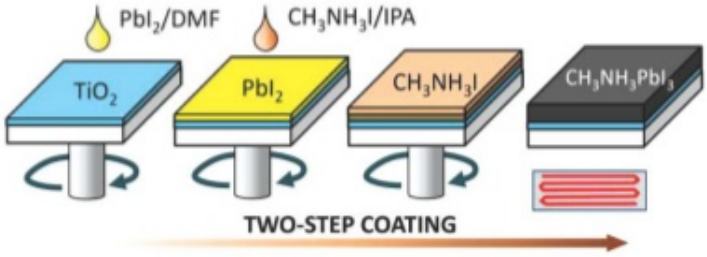

Figure 2.13 Schematic description of a two-step process. From ref. [19].

2.7.3 Other methods

Dual source vapour deposition: Salau first performed this technique to deposit a thin film of perovskite (PbI_2:KI) [23]. In 2013, Liu and colleagues [24] obtained a perovskite solar cell by vapour deposition: the organic and the inorganic precursor are evaporated at the same time with an as-deposited non-stoichiometric molar ratio. An annealing treatment in inert atmosphere is carried out after the evaporation in order to enable the complete crystallization of perovskite.

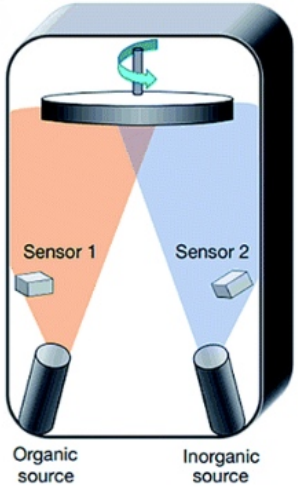

Figure 2.14 Schematic description of a dual-source vapour process. From ref. [25].

Vapor-assisted solution process can be seen as a combination of the sequential deposition and dual source vapor technique. A solid/vapor reaction step (exposing the PbI_2 film to the MAI vapor) was developed as an alternative to replace the regular MAI solution soaking step. This solid/vapor two-step conversion approach was first demonstrated by Yang and co-workers to prepare high-quality, pinhole-free planar $MAPbI_3$ films [25].

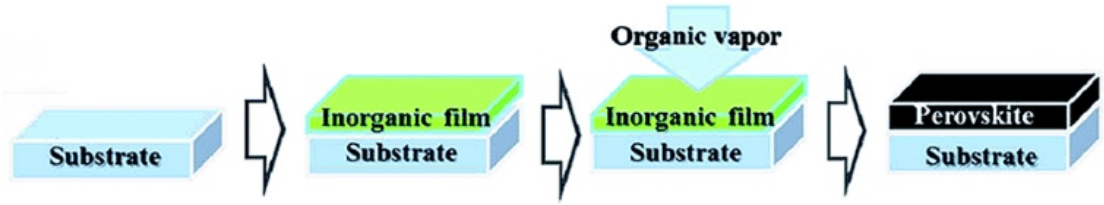

Figure 2.15 Successive steps in a vapor assisted solution process. From ref. [25].

2.8 Toward large scale Roll-to-Roll production

Recently, a PCE of more than 21% has been reported for solution-processed perovskite solar cells. Although rapid progress has been made, it was predominantly by the non-scalable process of spin coating. Spray coating was used to print perovskite solar cells, but only for perovskite layer [31]. Even though the coating method is a scalable process, it was impractical for use in the production of solar cells due to material loss as well as the low resolution

patterning that is insufficient for a module structure. Inkjet printing was used to convert spin-coated PbI_2 layer to perovskite layer and to print carbon electrodes [28]. The process is promising as it is scalable and vacuum free. However, it will be more ideal if all layers can be printed. The device structure of planar perovskite solar cells is similar to that of OPVs (Organic Photovoltaics). Therefore, the processes developed for OPVs should be adaptable. For the roll-to-roll fabrication of OPVs, many coating/printing methods such as slot-die coating, knife coating, spray coating, screen printing, gravure printing, flexographic printing, and inkjet printing have been studied [28]. Among the roll-to-roll compatible methods, slot-die coating has achieved the most success in the large-scale production of OPVs [29, 30].

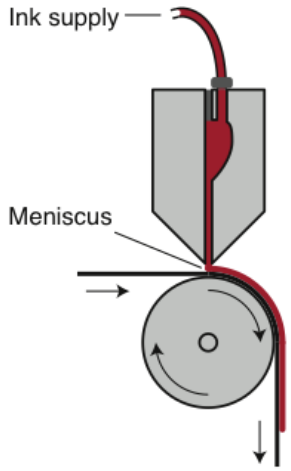

Figure 2.16 Principles of slot die coating. From ref. [63].

The process produces a uniform stripe with well-defined edges. Target film thickness can be easily achieved by controlling the solution feed. In addition, this process has no loss mechanism, and all injected solutions can be transferred to the substrate [29, 32].

Hwang and co-workers demonstrate the fabrication of fully slot-die coated perovskite solar cells. With the exception of evaporated metal electrode, all layers were fabricated via scalable process, slot-die coating [35]. The device configuration used is ITO/ZnO/$CH_3NH_3PbI_3$/P3HT/Ag for a planar architecture. The most difficult factor in translating the spin coating process to other scalable coating/printing methods was the different drying mechanisms. In the spin coating process, the solution spreads as soon as the substrate spins and then

the wet film dries while spinning at a very high speed. Therefore, there is a “quenching” step in the process. Most coating/printing methods form a wet film first, which is then allowed to dry naturally or by the use of a hot air dryer [29]. With such a slow drying step, however, the solution can flow and lose uniformity depending on the material [32, 33, 34]. They encountered more serious problems with the PbI_2 coating process, which consists of only small ions that rapidly form crystals. During a slow drying step, the small ions can migrate easily and form overgrown crystals, which mean that some areas on substrates are devoid of material and pinholes are formed. They introduced an external “gas quenching”: they attached an additional slot-die head to the original slot-die head for coating as shown in Figure 2.19. The second head was connected to high-pressure nitrogen to quickly dry the PbI_2 film. They obtained a more dense and uniform film, which could be converted to perovskite film. The completed device showed typical solar cell behaviour. As a result, the best *PCE* of 11.96% was obtained.

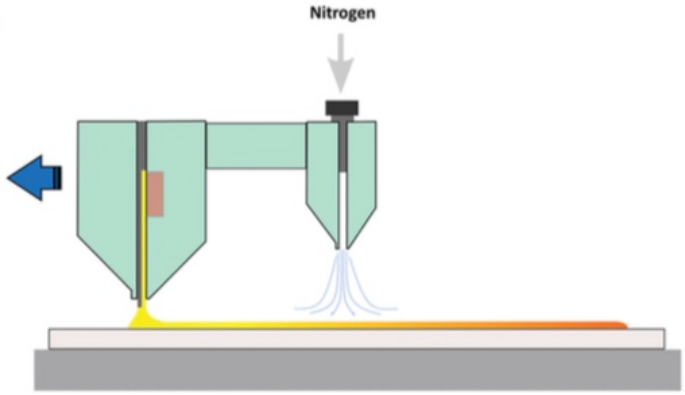

Figure 2.17 Schematic illustration of slot-die coating with a gas quenching process. From ref. [35].

2.9 Barcoating

A deposition method that has not yet been used for the perovskite solar cells fabrication is the barcoating. The barcoating is the printing deposition technique that will be used in this thesis work. A typical bar-coating machine consists of a coating bar sitting above a substrate (flexible or rigid), and a moving mechanism that enables the coating-bar to move against the fixed substrate. The process contains three major steps: 1) the horizontal transport of the coating bar against

the substrate, 2) the wet coating of the polymer film, and 3) the film drying. The grooves between the wire coils wound around the bar (Fig. 2.20) determine the amount of coating solution that will pass through as it moved along the substrate.

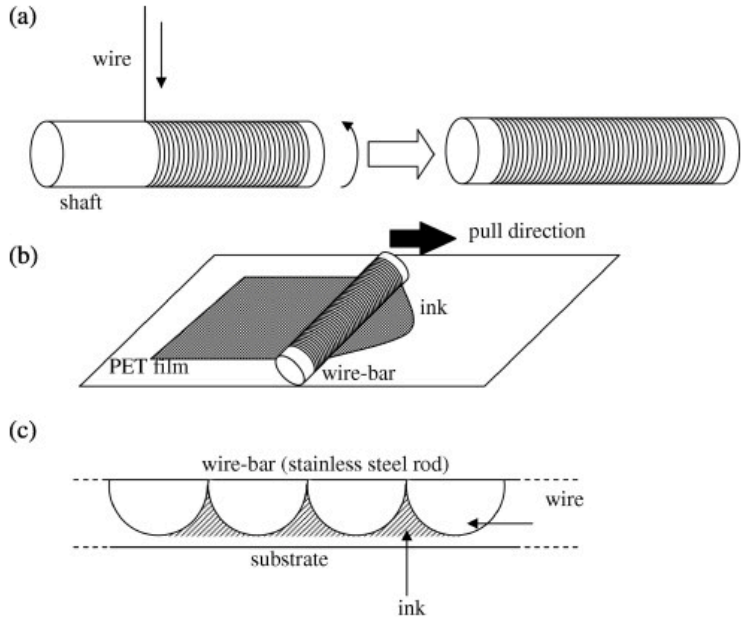

Figure 2.18 (a) Structure of wire-bar, (b) schematic diagram of wire-bar coating, and (c) side view of (b). From ref. [61].

The thickness and quality, i.e., roughness and uniformity, of the deposited films are mainly determined by a variety of experimental factors which can be easily controlled: viscosity of the solvent, pressure that the bar exerts on the substrate, speed of the bar. When the bar is lowered to achieve the most proximate contact between the bar and substrate, a small amount of solution passes through the gaps between the wound wires (Fig. 2.20c). Therefore, the thickness of the wet film is directly proportional to the diameter of the wire.

Chapter 3

Materials and methods

In this chapter an overview on materials and methods employed in this thesis for devices realization and characterization will be provided. S*ection 3.1* covers the materials used and the reasons that led to their selection, are presented. *Section 3.2* provides a synthetic description of the laboratory instruments and processing steps used in this thesis work for layers deposition. *Section 3.3* describes the experimental setup chosen for device characterization.

3.1 Materials

The purpose of this thesis is to find a new printing method that leads to the fabrication of low-cost devices. Before lowering the costs of the processes, it is necessary to find performing before lowering the costs of the processes you need to find materials which are performing and inexpensive at the same time. In this section the materials chosen and used for the fabrication of the devices are described.

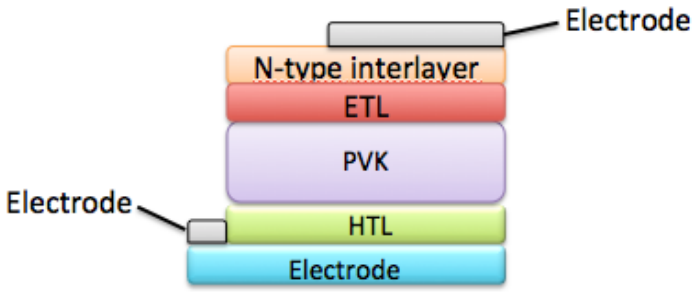

Figure 3.1 Device structure

3.1.1 Hybrid perovskite layer

The organic-inorganic halide perovskite layer is deposited through two different processing techniques: one-step deposition and two-step deposition (described previously in 2.8.1 and 2.8.2 section, respectively).

One-step deposition: the precursor solution for perovskite crystal is prepared by mixing powder of methylammonium iodide (MAI) and Lead (II) chloride ($PbCl_2$), at 3:1 non-stoichiometric mole ratio. The solvent used is N,N-dimethylformamide (DMF).

Two step deposition: the two solutions used are Lead (II) iodide (PbI_2), dissolved in N,N-dimethylformamide (DMF) and methylammonium iodide (MAI) in anhydrous isopropanol (IPA).

3.1.2 Hole Transport Material (HTL)

To improve the ITO-active layer interface the most used material is by far PEDOT:PSS, a water soluble polymer composed by the mixture of two ionomers: poly(3,4-ethylenedioxythiophene) (PEDOT) and Sodium polystyrene sulfonate (PSS).

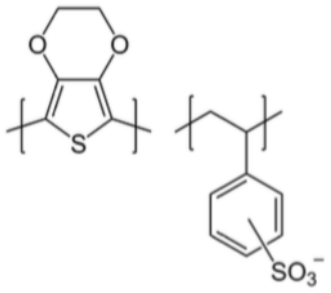

Figure 3.2 PEDOT (on the left) and PSS (on the right) molecular structure.

This material shows many promising properties as interlayer: (1) it has a high optical transparency in the visible range; (2) it is effective in transporting holes to the anode and in blocking electrons; (3) its high work function, around 5 eV, allows the formation of an ohmic contact with most of the donor polymers; (4) it helps to planarize ITO surface, providing better electrical contact; (5) it is stable in ambient conditions [59]. The drawback is that due to the acidic nature of PEDOT:PSS, the realized devices are unstable: ITO is etched with time and the active layer is damaged. Other materials have been used for the same purpose (polythiophene [45], spiro-OMeTAD [46], graphene oxide (GO) [47], NiO [48, 49], V_2O_5 [48] and CuSCN [50]), but PEDOT is still the best performing and reproducible.

3.1.3 Electron Transporting Material (ETM)

Fullerene (C_{60}) and its derivatives are the most widely used n-type materials for ETLs in inverted perovskite solar cells. The most commonly used fullerene derivatives, Phenyl-C_{60}-butyric acid methyl ester ($PC_{61}BM$), could effectively quench the photoluminescence of $CH_3NH_3PbI_3$, suggesting a high probability of efficient charge transfer [36]. Apart from $PC_{61}BM$, other fullerene compounds have been used in similar device configurations: C_{60}, ICBA and $PC_{71}BM$.

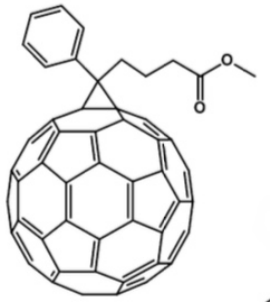

Figure 3.3 $PC_{61}BM$ structure.

3.1.4 N-type interlayer

Traditionally upper interlayer is not used in OPVs due to interaction with the active layer during deposition and to difficulties in finding suitable low work function materials. In the last years however, altogether with the introduction of inverted structure, different hole blocking layers (HBL) have been developed and used (TiO_2 [48, 51], AZO, BCP [52], ZnO [47], Ca [52, 53], LiF [54], C_{60} and its derivatives [55, 56]). We selected the Alluminum Zinc Oxide (AZO): ZnO nanoparticles doped with Alluminum in isopropanol (IPA).

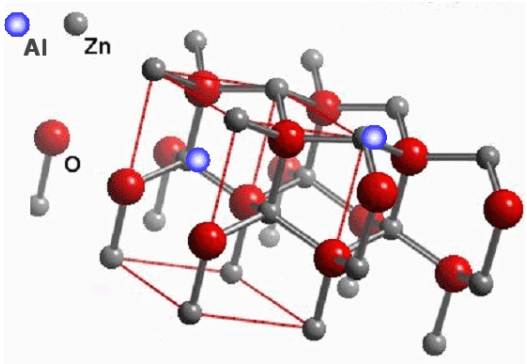

Figure 3.4 AZO structure.

3.1.5 Electrodes

Main requirements for electrodes are low sheet resistances (measure of resistance in thin film [Ω/sq]) and work functions matched with donor's HOMO and acceptor's LUMO in order to provide Fermi level pinning and thus good ohmic contacts. Being that light should reach the active layer of the cell, one of the electrodes should be transparent in the absorption window of the active

material. Since metals are all strong absorbers for visible radiation, transparent conductive oxides TCO are generally used as substitutes [57]. Indium Tin Oxide (ITO), with a work function lying between 4.4 - 4.8 eV [58] still represents the best trade off between transparency and conductivity. We used aluminum, with a WF of around 4.3 eV, for cathode realization, due to the low cost and to the well matched work function. Silver and gold can be used for the same purpose but they are more expensive and even a very small interlayer defect leads to a significant loss of performance (decoupling effect).

3.2 Methods

Here the steps for device's realization are presented, along with the instruments employed in devices' realization.

3.2.1 Solution preparation

For the PbI_2 preparation, the PbI_2 powder was placed in a clean vial with a stirrer and weighted; the solvent (DMF) was then added according to the desired concentration (200, 300, 400, 600 mg/ml) and the suspension was left on an hotplate heating plus stirring at 90°C, 800 rpm till complete solution (usually 20 min). For the MAI preparation, the MAI powder was placed in a clean vial with a stirrer and weighted; IPA was added as a solvent according to the desired concentration (4, 10, 16, 40 mg/ml) and the suspension left on the hotplate heating plus stirring at 70°C, 800 rpm till complete solution (usually 20 min). For PCBM preparation, the PCBM powder was placed in a clean vial with a stirrer and weighted; the solvent (CL, chlorobenzene) was added according to the desired concentration (20 mg/ml) and the suspension left on the hotplate heating plus stirring at 70°C, 800 rpm over night. For the precursor solution of perovskite crystal for the one-step deposition ($CH_3NH_3PbI_{3-x}Cl_x$) the MAI powder was placed in a clean vial with a stirrer and weighted. Then $PbCl_2$ was weighted using a second vial in order to obtain a non-stoichiometric ratio of 3 (MAI): 1($PbCl_2$). The solvent (DMF) was added in the MAI vial and the suspension left on the hotplate heating plus stirring at 90°C, 800 rpm till complete solution. Once complete

solved, the solution (including the stirrer) was transferred in the $PbCl_2$ vial and left on the hotplate heating plus stirring at 90°C, 800 rpm for three hours.

3.2.2 Substrate preparation

The substrate used is a 2.5x2.5 cm^2 glass, with a central ITO-covered stripe having a width of 8 mm and a sheet resistance of 15 Ω/sq. Each substrate is engraved on the back with a cross using a diamond pen. In this way four different devices can be obtained from a single substrate. Before deposition of any layer, eventual organic contaminants should be removed from the surface. For this purpose a multi-step cleaning is carried out under fume hood, exploiting sonication at 100% power of the substrates in different solvents: (1) acetone (5-10 min), (2) IPA (5-10 min), (3) acetone (5-10 min), (4) IPA (5-10 min). After the last cleaning cycle the substrates were immediately rinsed with nitrogen to avoid re-adhesion of impurities on the wet surfaces. To improve the surface's wetting and to remove organic contaminants the substrate a plasma treatment is done. Devices are placed in a Diener Femto plasma system [60], exposing the ITO face, in an oxigen atmosphere and treated for 10 min at 100% forward power.



Figure 3.5 The BRAINSON 2510 sonicator used is shown on the left of this figure, while on the right is shown the Diener plasma system.

3.2.3 Layer deposition

All the layers (except the top electrode) have been deposited via spin coating (in air or glovebox conditions), or via barcoating in air. As described before, the starting substrate can be divided into four parts. The different substrates are divided at different times, depending on the deposition method used. When all the layers are deposited by spincoating, the substrate is divided into four immediately after the PEDOT:PSS deposition. On the other hand, all the printed layers are deposited on the big initial substrates, which are separated just after the print step.

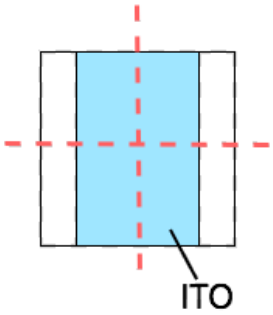

Figure 3.6 Schematic representation of the substrate.

Spincoating

The substrate is placed on a rotary holder and kept in place through air suction. The layer-forming process can be split in four steps:

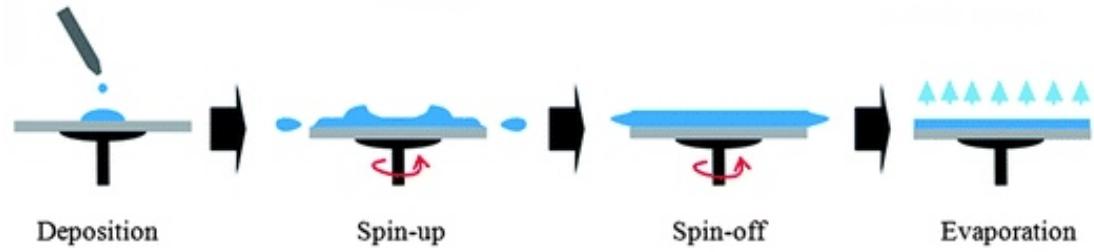

Figure 3.7 Schematics of the four main spin coating steps.

1) Deposition: a small amount of solution, exceeding the need for layer formation, is deposited on the substrate.

2) Spin up: a rotational acceleration is applied to the holder, spreading liquid over the underlying surface. Main part of the fluid is expelled from sample because of the speed up and a thin film with homogeneous thickness eventually forms. Ultimately, the wafer reaches desired speed and the fluid becomes thin enough to allow viscous shear drag for balancing the rotational acceleration.
3) Spin-off: the holder is spinning at a constant rate and layer's thinning is dominated by viscous forces. Droplets of liquid are flung off at glass' sides and edge effects, caused from the expulsion, can be observed.
4) Evaporation: the speed is kept constant and layer thinning is dominated by solvent evaporation. Viscosity of the layer increases along with progression of the evaporation process.

Critical aspects to be controlled for device's realization through this method are: a proper substrate wetting (to avoid non-uniform coverage), absence of undissolved particles (can be removed by filtering) and control of border effects, which can be relevant especially in small samples. When spin coating multiple layers the use of solvents interacting with the underlying film should be avoided, to prevent damages to the layer surface. All spin coating steps have been realized under fume hood or in glovebox with a Laurell WS-400BZ-6NPP/LITE [92].



Figure 3.8 Image of the Laurell spin coater used for layer deposition.

Barcoating

For this thesis work a TQC barcoater is used.

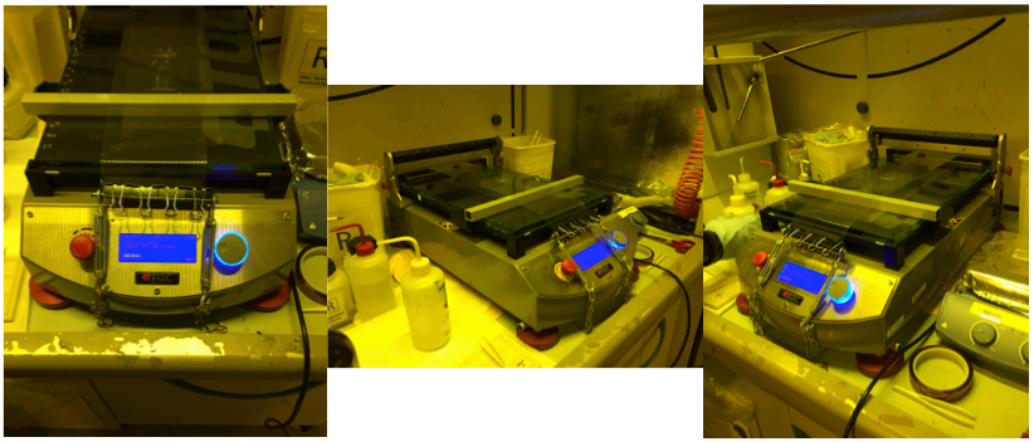

Figure 3.9 TQC barcoater images.

Process step by step:

1) Preparation of the support for the substrate: a pet sheet is applied with scotch tape at the two ends of the barcoater in such a way that it does not touch the base. This is done to have a non-rigid support for the substrate. With this configuration there is a softer passage of the bar on the substrate. Therefore the possible sample scratching due to the pressure of the bar is avoided.

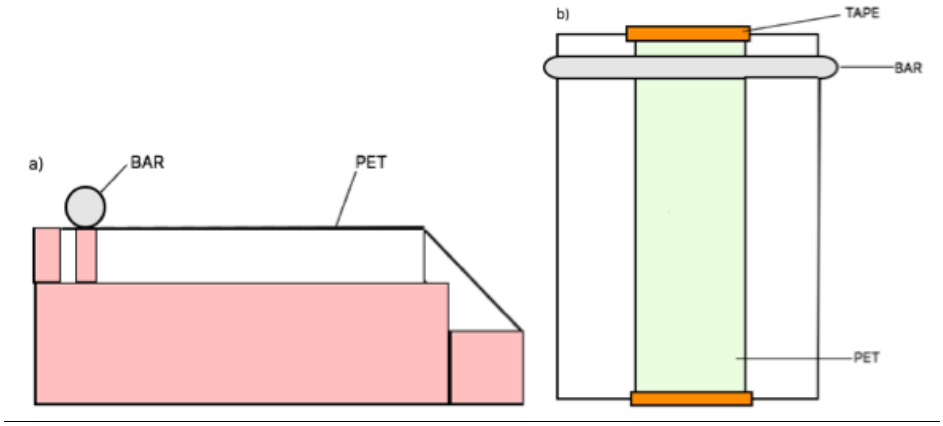

Figure 3.10 PET positioning on the barcoater, a) side view, b) top view.

2) Positioning of the substrate: above the pet sheet, an absorbent paper rolled up at the end is positioned and attached with tape to ensure that

the excess solution not return on the substrate. The substrate is then positioned with carbon tape as in the figure below.

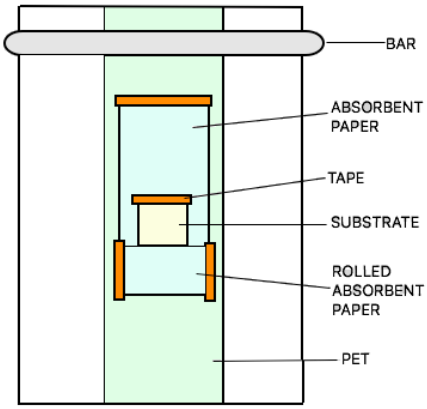

Figure 3.11 Schematic representation of the positioning of the different elements: absorbent paper, tape and substrate.

3) Parameters setting: select and insert the desired speed value (mm/s) and vary the pressure on the substrate by varying the height of the bar.
4) Coating: put the required amount of solution for coating directly on the initial part of the substrate (see fig. 2.23) and press the start command immediately to avoid too much contamination of the solution due to the exposure to air.

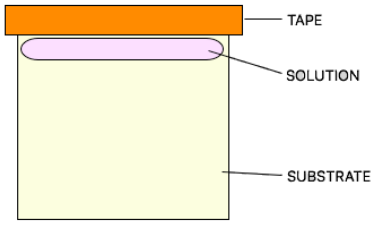

Figure 3.12 Schematic representation of the positioning of the solution.

5) Gas quenching: as already mentioned in the previous section, a nitrogen flux is needed to allow a good drying of the film. Lacking a machine to be able to do so, the nitrogen gun of the fumehood is used. The flow is directed, slowly and about 4 cm away, from the tape to the end of the substrate just after the transition of the bar. Thus the nitrogen flux follows the bar movement. The drying lasts approximately 15 seconds.

PEDOT:PSS

The solution of PEDOT:PSS was deposited (in air) at T_{amb} (about 23-25°C) or at 60°C depending on the type of experiment. Few drops of solution have been deposited (through a 0.2 µm PVDF filter) on the freshly cleaned substrate (plasma treatment should be done immediately before spin coating the solution, to avoid reformation of the oxide layer) and spin coated for 1 minute at 2500 or 5000 rpm (round per minute) with maximum acceleration depending on the type of experiment. After deposition, PEDOT:PSS has been thermally treated (annealed) by heating it on an hotplate at 150°C for 10 minutes. The annealing step is needed to remove water leftovers and to hinder the acidic behaviour of PEDOT.

PbI_2

Via spincoating (in glovebox): the solution of PbI_2 was deposited at 70°C. Few drops of solution have been deposited on the PEDOT:PSS layer and spin coated for 35 seconds at 2000 or 4000 rpm with 2000 acceleration depending on the type of experiment.

Via barcoating (in air): the solution of PbI_2 was deposited at 70°C. Few drops of solution (0,40 µl, or 0,60 µl depending on the type of experiment) have been deposited on the PEDOT:PSS layer. A bar height of 20 nm and a speed of 50 mm/s were chosen, providing the best uniformity of the layer. The gas quenching step in then provided to make the evaporation faster and decrease the amount of oxygen in contact with the layer.

In both cases, after deposition, PbI_2 has been annealed by heating it on a hotplate at 70°C for 15 minutes.

MAI

The solution of MAI was deposited (in glovebox) at T_{amb} (about 23-25°C) on the substrate with the PbI_2 layer. Few drops of solution have been deposited and spin coated for 35 seconds at 2000 rpm (round per minute) with 2000 acceleration. After deposition, MAI has been annealed by heating it on an hotplate at 100°C for 90 minutes to start the interdiffusion process.

K330

Via barcoating (in air): the solution was deposited at 70°C. Few drops of solution (0,60 µl) have been deposited on the PEDOT:PSS layer. The bar height was set at 20 nm. The bar velocity was set again at 50 mm/s. After deposition, the substrate has been annealed in four different conditions:

1. 30 min in air @T_{amb} + 90 min in air @90°C
2. 30 min in air @T_{amb} + 30 min in air @90°C + 60 min in glovebox 90°C
3. 30 min in air under a N_2 hood @T_{amb} + 90 min in air @90°C
4. 30 min in air under a N_2 hood @T_{amb}+ 30 min in air @90°C + 60 min in glovebox 90°C

These different annealing conditions were made to see the effect of atmosphere conditions on the final performance of the device.

PCBM

The solution of PCBM was deposited (in glovebox) at T_{amb} (about 23-25°C). Few drops of solution have been deposited (through a 0.2 µm PTFE filter) on the perovskite layer and spin coated for 50 seconds at 2000 rpm with 2000 acceleration. After deposition, PCBM has been annealed by heating it on an hotplate at 90°C for 20 minutes.

AZO

The solution of AZO was deposited (in glovebox) at T_{amb} (about 23-25°C). Few drops of solution have been deposited on the PCBM layer and spin coated for 50 seconds at 2000 rpm with 2000 acceleration. After deposition, AZO has been annealed by heating it on an hotplate at 90°C for 20 minutes.

Al-Electrode

Before proceeding with the evaporation, a sample area is fully scratched away to allow the contact between the two electrodes. The mask used for the Al deposition allows the formation of three horizontal and one vertical contacts. Thus each device has three different pixels. The active area of each pixel is measured (0.08 cm^2).

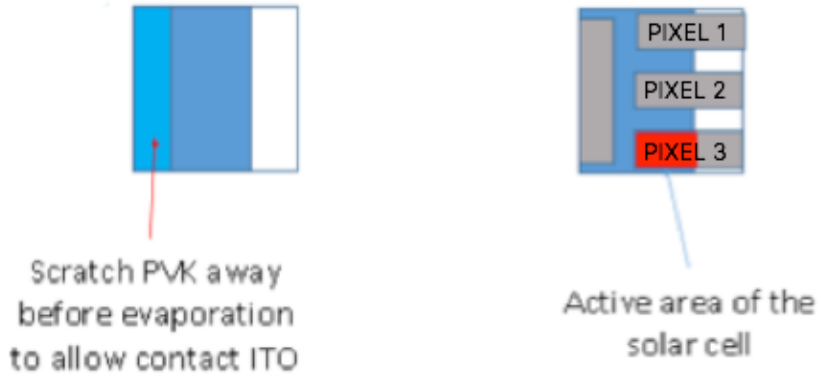

Figure 3.13 Schematic representation of the scratched area (on the left) and the active area and the different pixels (on the right).

The aluminum electrode has been deposited via evaporation: devices were brought in a MB-ProVap-3 evaporator inside glovebox (MBRAUN, MB200B) and brought to 10^{-6} mbar. Aluminium was melted inside a Tantalum boat, heated through electric flow, and evaporated. When a stable deposition rate higher than 0.2 Å was reached, the substrate shutter, used to protect samples in the previous part of the process, was removed, thus allowing Al deposition. Around 100 nm thick layer has been deposited in all the devices. Before the characterazation, silver paste was used to improve contact between the applied legs of the Solar Simuletor and the evaporated Al.

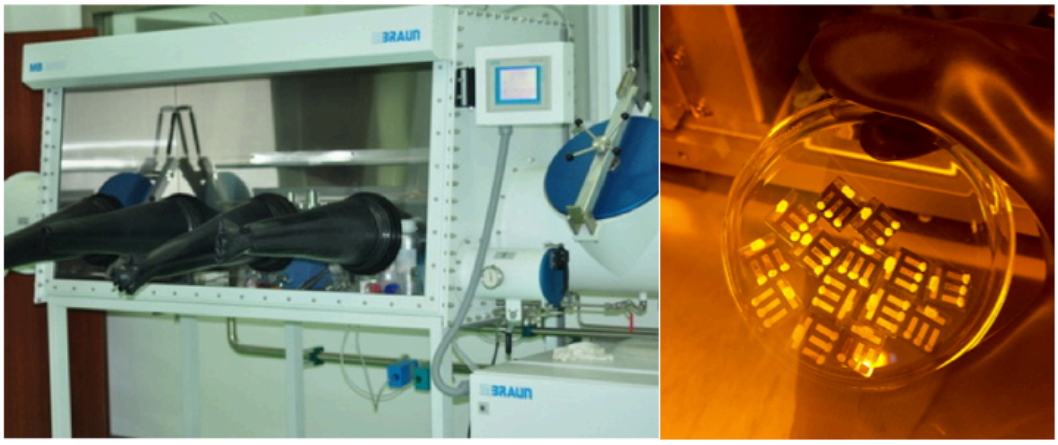

Figure 3.14 Image (on the left) of the MBRAUN glovebox used for evaporation, annealing and spincoating and (on the right) the appearance of the complete devices.

3.3 Characterization

Different analyses were done on devices, to achieve electrical and morphological characterization. In this section the measurements and experimental setups employed are presented.

3.3.1 J-V under illumination

The light characteristic that has been measured for all the devices is AM 1.5. Illumination in this stage has been provided from an Oriel Solar Simulator. The setup is composed of a computer with Oriel IV test station software, for data elaboration, a multimeter (Keithley 2440 5A Source Meter), for data acquisition and a substrate holder with a switch, to provide selective cathodic contact for the solar cells realized in each device. To acquire the J-V characteristic ITO has been fixed to ground and a voltage sweep has been applied to the cathode, exposing device under the solar simulator light cone.

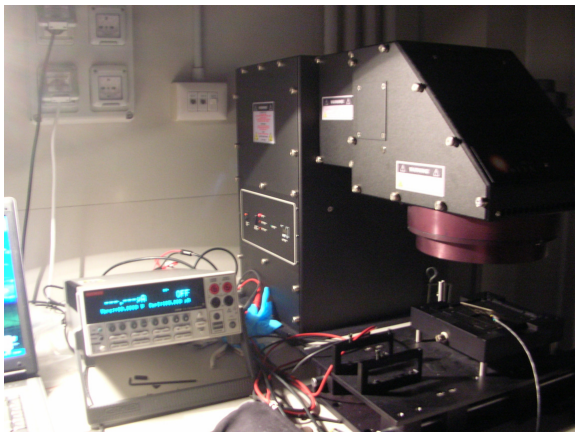

Figure 3.15 The measurement setup is shown in the picture, with the sample holder positioned under the illumination source and connected to the Keithley 2440 5A source meter.

3.3.2 Layers thickness

Incomplete devices has been used for the measurement: a single layer was deposited on clean glass (eventually annealed) and scratched, to expose the underlying substrate. A contact profilometer (Veeco Dektak 150) has been used for the characterization: a scanning tip, provided with a capacitive transducer, for the measurement of vertical displacement, was moved along the sample's

surface and across the scratch. The difference between average film and glass heights provided then the layer thickness.



Figure 3.16 Veeco Decktak 150 profilometer.

3.3.3 Surface Morphology

In order to get a complete device characterization, Scanning Electron Microscope (SEM) has been used. A scanning electron microscope (SEM) is a type of electron microscope that produces images of a sample by scanning it with a focused beam of electrons. The electrons interact with atoms in the sample, producing various signals that contain information about the sample's surface topography and composition. The electron beam is generally scanned in a raster scan pattern, and the beam's position is combined with the detected signal to produce an image. SEM can achieve resolution better than 1 nanometer.

3.3.4 Crystallinity

To discover the final components of the deposited film, an XRD analysis has been used. It is based on constructive interference of monochromatic X-rays and a crystalline sample: The X-rays are generated by a cathode ray tube, filtered to produce monochromatic radiation, collimated, and directed toward the sample. The interaction of the incident rays with the sample produces constructive interference of the diffracted rays when conditions satisfy Bragg's Law ($n\lambda=2d \sin$

θ). This law relates the wavelength of electromagnetic radiation to the diffraction angle and the lattice spacing in a crystalline sample.

The characteristic x-ray diffraction pattern generated in a typical XRD analysis provides a unique “fingerprint” of the crystals present in the sample. When properly interpreted, by comparison with standard reference patterns and measurements, this fingerprint allows identification of the crystalline form.

Chapter 4

Hybrid perovskite morphology optimization

The performances of perovskite based solar cells are highly dependent on film morphology. The filming and crystallization processes in these materials are highly variable and sensible to many different parameters. Some of the most critical parameters influencing film morphology are: deposition method, material composition, temperature, humidity, atmosphere conditions and film treatment. For high-performance planar heterojunction solar cells, it is essential to have nearly complete surface coverage to prevent both low-resistance shunting paths between the n- and p-type contacts, as well as low light absorption in the solar cell. Furthermore, factors such as charge dissociation efficiency, charge transport and diffusion length of charge species are dependent on the crystallinity of the film (grain dimensions, compactness, presence of defects). After all, also the humidity plays an important role: humidity has been shown to be detrimental to the performance of the cells [98] because of the hygroscopic nature of CH_3NH_3 (as mentioned before in section 2.7). With the final aim of optimizing the morphology of a printed layer, a study on morphologies has been carried out, controlling the thicknesses of the deposited layers, the morphologies (SEM) and the quality of the grains (XRD). In a first step a study on films deposited by spin coating has been carried out then some attempts have been done for film deposition with a scalable technique.

4.1 Lead Iodide (PbI_2)

The morphological difference obtained by different deposition methods appears to be the major problem to switch from laboratory to industrial scale. In this chapter the Lead Iodide layer futures obtained via spincoating and barcoating are described, analysed and optimized.

4.1.1 Spincoating (in glovebox)

The most important factors affecting the output of the spin coating technique are the concentration of the solutions which are involved in the process, as it determines the amount of chemical species that are deposited on the top of the substrate and so the thickness of the film, and the spin rate, because it controls in a more direct way the thickness of the layer of solution. The impact of the change in the spin rate for the deposition of PbI_2 is evaluated by comparing the different thickness obtained.

To achieve a complete reaction of the PbI_2, the layer thickness should be about 150 nm [99]. This is because a too much thick PbI_2 layer would not allow the MAI to penetrate until the bottom and too long annealing time would be required (2 or 3 hours instead of 90 minutes [81]). This would lead to too long process times and therefore to the increase of production costs.

A first rough selection of the spin coating parameters has been done by simply comparing the thicknesses of the lead iodide layers. In table 3.1 it can be noted which is the thickness obtained by the different proceedings. The measurement was made on different points of the substrate and the maximum thickness variation is of 2 nm (in the barcoater case the variation will be grater).

Sample	Solution concentration (mg/ml)	Rpm, acceleration	Thickness (nm) (±2)
1	400	2000, 2000	303
2	300	2000, 2000	226
3	200	2000, 2000	178
4	400	4000, 4000	266
5	300	4000, 4000	195
6	200	4000, 4000	132

Table 4.1 Spin parameters, solution concentrations and thickness of different samples.

The samples that are closest to the ideal thickness value are: 3, 5, 6.

From the SEM image of the sample 3 (fig. 3.1), it can be noted that the PbI_2 layer deposited is fairly homogeneous. For these reasons a concentration of 200 mg/ml and spin speed of 2000 rpm and 2000 acc. have been chosen as starting points for the following spin of MAI and conversion to PVK.

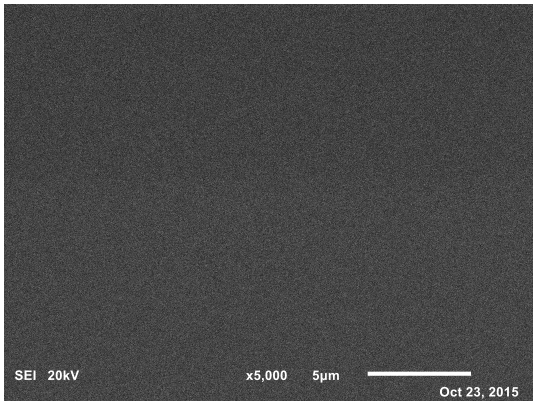

Figure 4.1 SEM images of Sample 3.

4.1.2 Barcoating:

The study over the morphology of the spin coated lead iodide layer has been required to have a reference and comparison in the following step towards large scale deposition. Unlike the spincoting, the barcoating procedure is done entirely

in air conditions. The operation in glovebox is not possible due to solvent saturation that will change every time the morphology due to a cross contaminations with other solvents. The barcoater is just put under a fumehood to avoid lead and DMF contamination of the work area. As a consequence, the morphological control and the surface uniformity control result to be much more difficult due to the PbI_2 instability in air. The aim of the experiment is to obtain a fairly homogeneous surface with not too large PbI_2 crystals. Large crystals greatly decrease the accessibility of MAI to the inner lead sites, hindering its interdiffusion and resulting in incomplete conversion [81].

In this experiment the PbI_2 layer is deposited as described in section 3.2.3). The parameter that varies is the type of drying. The PbI_2 solution (400 mg/ml) is always maintained at 70°C. The substrate drying was made with the N_2 flux (as mentioned in section 3.2.3, “gas quenching”).

Here the different parameters for the different samples prepared are presented. In this case the thickness variation depends on the deposition method.

Sample	Substrate T (°C)	Solution quantity (µl)	Gas quenching	Thickness (nm)
1	23°C (ambient)	0,60	no	520±300
2	23°C (ambient)	0,60	yes	260±15

Table 4.2 Substrate temperature, solution quantity, quenching parameter and thickness obtained of different samples.

There's a huge quality difference between the lead iodide film deposited with or without gas quenching. The gas quenching turns out to be a critical step also from a morphological point of view. The naturally dried film shows insufficient surface coverage. On the other hand, the gas quenched film shows very good uniformity and smaller crystals. According to [35], the nitrogen flow induces the formation of a dense, dried skin. The use of the nitrogen flux speed up the solvent evaporation, and reduces the PbI_2 crystals reorganization after the film coating.

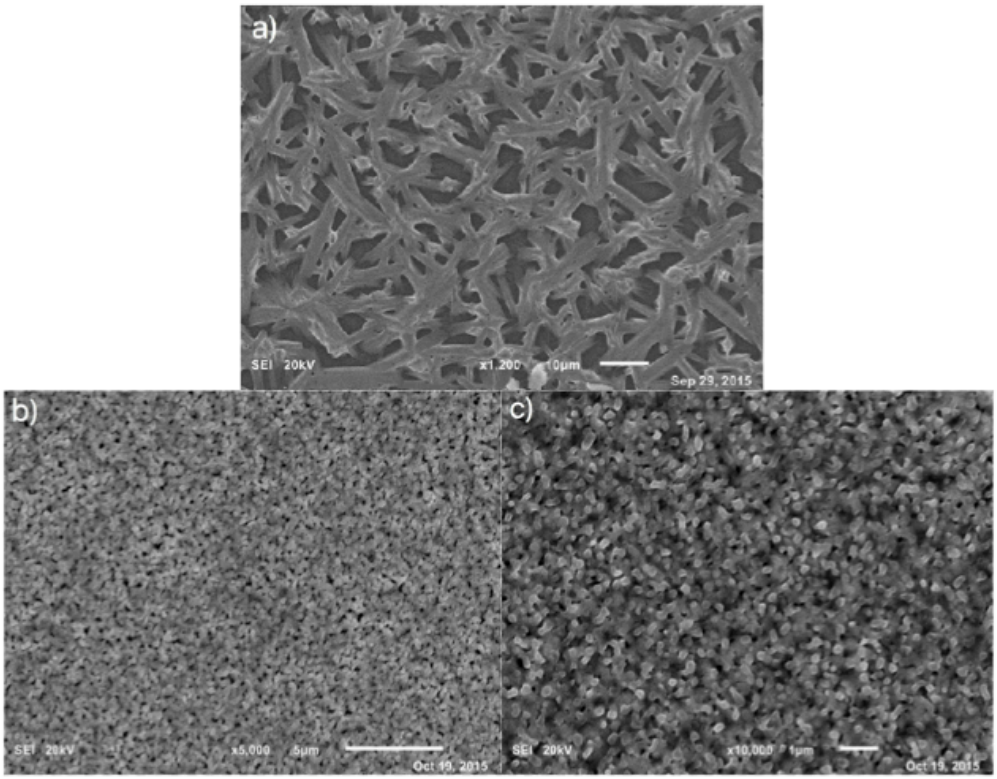

Figure 4.2 SEM images of a) sample 1 (no gas quenching), b) sample 2 (gas quenching), c) sample 3 at higher magnification.

The results obtained with this experiment are very promising. In fact Hwang and co-workers [35] have led to very similar morphological results, despite the equipment used are not of the same engineering level: the barcoater used is very simple, there's not a gas quenching equipment and the experiment was done in an uncontrolled atmosphere.

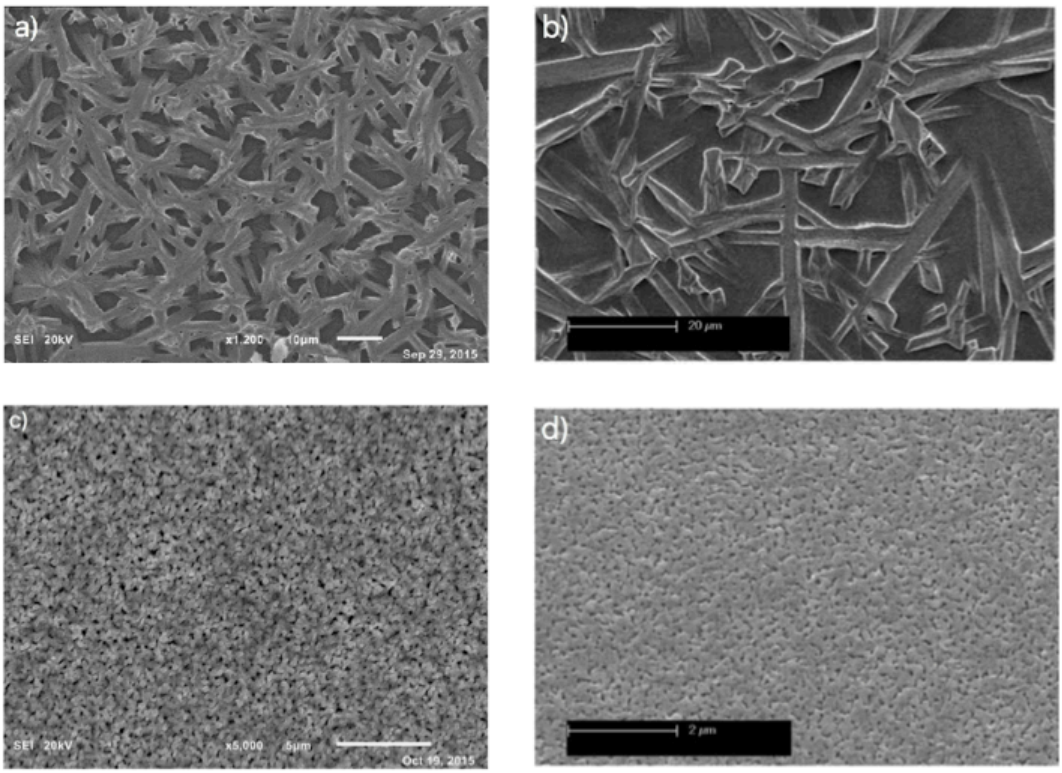

Figure 4.3 SEM images of a), c) this experiment, b), d) Hwang and co-workers experiment.

4.2 Methylammonium Iodide (MAI)

The optimization of the lead iodide layer is not sufficient to attain a good perovskite layer: for this reason the MAI deposition method was analysed and optimized.

4.2.1 Single step MAI deposition (Dyesol vs. Homemade)

A comparison between Dyesol methylammonium iodide (MAI) and synthesized MAI is made in order to determine the most valid precursor for deposition of halide perovskite $CH_3NH_3PbI_3$ through two-step deposition. The parameters of the spin coating process are not changed in order to define the contribution coming from the particular chemical species. Synthesized MAI is obtained by mixing 10 ml of methylamine solution (40% in weight in anhydrous ethanol) and 14 ml of hydroiodic acid (57% in weight in water). The reaction is performed in ice bath for 2h under magnetic stirring and the solvent is removed with a rotary

evaporator (1h at 60 mbar and 60°C). The product is purified by dissolution in ethanol and recrystallization with diethyl ether, where the washing cycle is repeated six times. After filtration, the resulting white powder is dried in a vacuum oven at 60°C for 24 h. In the SEM images it can be noted a significant difference: the formation of larger crystalline grains when the synthesized MAI is used, while Dyesol MAI yields smaller crystal domains. Another interesting aspect is the roughness of surface: synthesized MAI causes the formation of a rougher surface with respect to Dyesol MAI, which results in a compact layer, showing fewer asperities. The use of synthesized MAI does not lead to effective process scalability. The use of materials already on the market is necessary to decrease the costs and the production times. Despite the morphological improvement achieve with the synthesized MAI, the Dyesol one will be used for the devices fabrication.

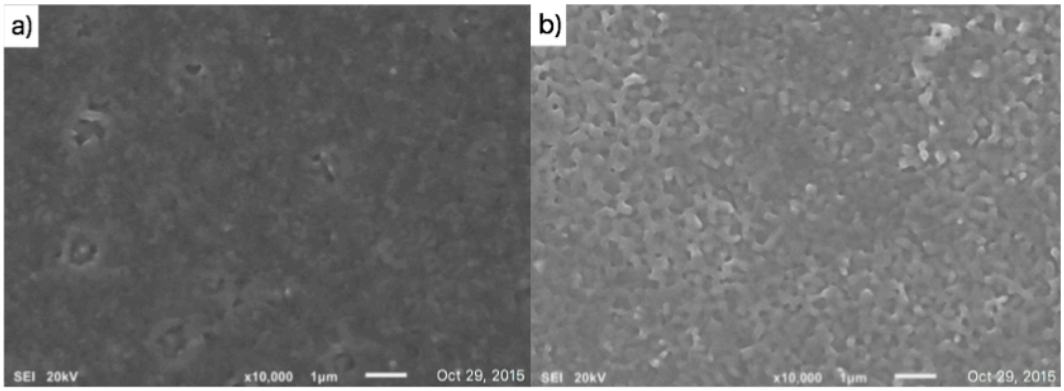

Figure 4.4 SEM image of the surface of perovskite layer obtained from a) Dyesol MAI and from b) synthesised MAI.

4.2.2 IPA cleaning

It has been frequently reported that the morphology of OTP films tends to be different in different laboratories, or in the same laboratory in different atmosphere conditions, even with the same film preparation procedure [77]. Here a SEM image of a perovskite layer obtained from a Dysol MAI is presented. All the deposition parameters are kept constant. Despite this, the surface is completely different from that presented previously (fig. 3.4a). The perovskite layer became blur and white precipitates were observed (fig. 3.5a). Probably these residues could be unreacted MAI or PbI_2 impurities [77]. Trying to make the

surface clearer and more homogeneous, the sample was washed with IPA (IPA cleaning) to remove the unreacted raw material (MAI) and/or the residual solvent. IPA was chosen because it's the MAI solvent. The washing procedure was done by spincoating: few drops of IPA have been deposited on the substrate with a 30 seconds loading time and then spin coated for 35 seconds at 2000 rpm with 2000 acceleration. The resulting surface (fig. 3.5b) didn't show halos. In addition to that, the white residues appeared to be less pronounced, but they were still present. Then it can be said that certainly the IPA cleaning step leads to a greater surface homogeneity and definition, but it didn't remove all the residues.

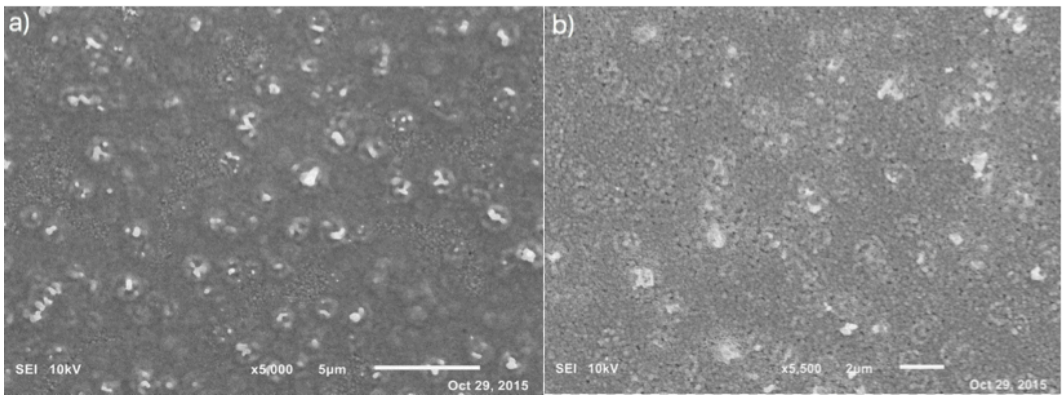

Figure 4.5 SEM images of a) perovskite layer obtained from a Dysol MAI and b) the same layer after IPA cleaning.

4.2.3 Double step MAI deposition

To ensure a complete conversion to perovskite throughout the whole film thickness and to have a better control of the crystallization process, a new successive spin coating/annealing process is used, where MAI (at different concentrations) is infiltrated twice into the PbI_2 film and followed by thermal annealing. The double deposition should lead to a better control of the perovskite morphology.

Spinned PbI_2

In the experiment all the samples present the same PbI_2 layer (2000 rpm, 2000 acc, 50 sec, 200 mg/ml) in order to define the contribution coming from the double MAI deposition. Both the MAI layers are deposited as described in section

3.2.3. In all the samples the second MAI deposition step is done with a 40 mg/ml MAI solution, while the concentration of the first step can be: 4 mg/ml, 10 mg/ml or 16 mg/ml. Between the two steps, the sample is annealed by heating it on an hotplate at 100°C for 5 minutes. The experiment was done using both types of MAI (Dyesol and synthesized) in order to check again the data presented in the previous section ("Dyesol MAI vs. synthesized MAI"). Here the different parameters for the different samples prepared are presented.

Sample	**MAI (mg/ml)**		
	MAI type	**1st step**	**2nd step**
1	Dyesol	4	40
2	Dyesol	10	40
3	Dyesol	16	40
4	Synthesized	4	40
5	Synthesized	10	40
6	Synthesized	16	40

Table 4.3 MAI type, first step concentration and second step concentration of different samples.

Now the image of the samples will be presented. In the Dyesol MAI case (fig. 3.6 a,b,c) there are still many residues, especially in the samples 2 and 3 (fig. 3.6 b,c). The surfaces are not perfectly clear. The positive aspect is that the perovskite grains are perfectly visible due to the fact that with a double MAI deposition the PbI_2 can react almost completely. In the synthesized MAI case (fig. 3.6 d,e,f) the perovskite crystals are better defined and there aren't white residues.

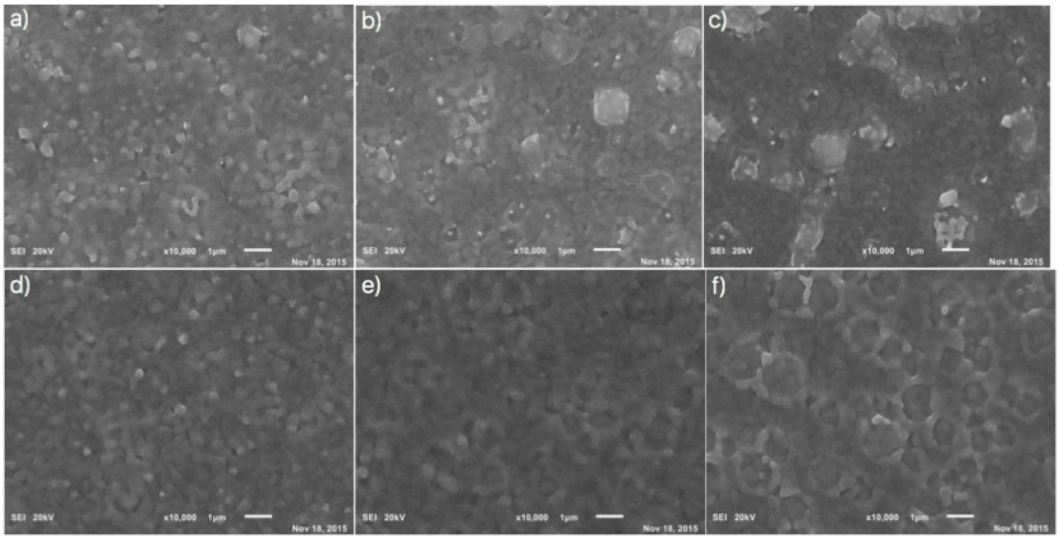

Figure 4.6 SEM images of the samples a)1, b)2, c)3, d)4, e)5, f)6.

Comparing the image of perovskite films obtained with a MAI single step deposition (fig. 3.7 a,c), it can be noted that the perovskite films obtained with the double step MAI (fig. 3.7 b,d) deposition are more homogeneous with greater and more defined perovskite grains. This confirms the fact that the PbI_2 is converted more efficiently to perovskite. This is a really positive aspect because the greater the grain size, the smaller the number of grain boundaries and thus the number of possible defects. There is also a better charge transport and a better film compactness.

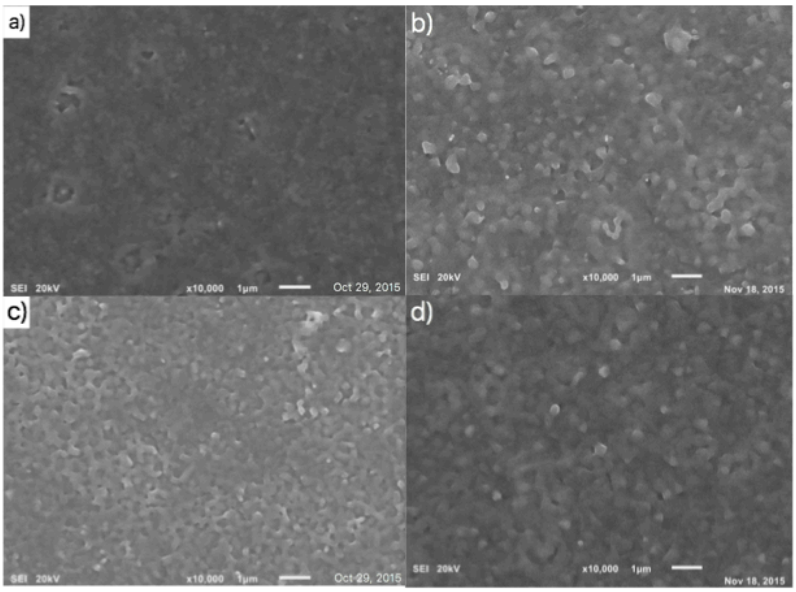

Figure 4.7 SEM images of perovskite layers obtained from a)one step Dyesol MAI deposition, b)double step (4+40 mg/ml) dyesol MAI deposition, c)one step synth. MAI deposition, d) double step (4+40 mg/ml) synth. MAI deposition.

The washing procedure (“IPA cleaning”, described previously) was also done on the six perovskite layers obtained from the double step MAI deposition (fig. 3.8) in the attempt of removing eventual MAI leftovers due to the introduction of a further MAI spincoating step. As previously observed, the introduction of a washing step leads to the formation of a smoother film with greater homogeneity and definition.

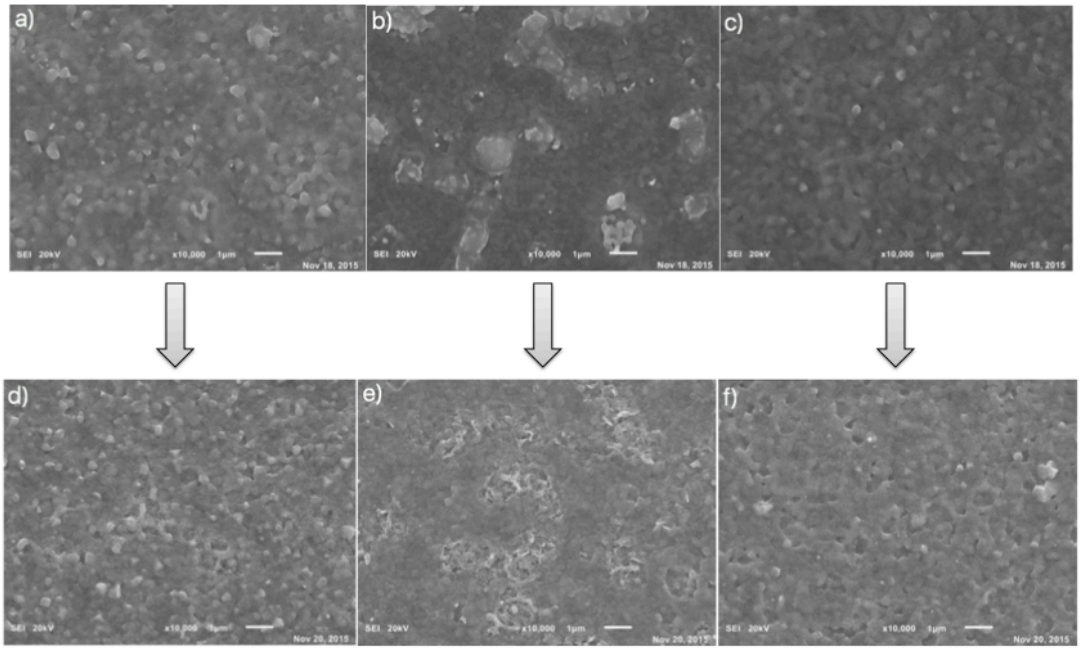

Figure 4.8 SEM images of samples (reported in table 3.3) number a)1 (before IPA cleaning), b)3 (before IPA cleaning), c)4 (before IPA cleaning) and the corresponding after IPA cleaning (d, e, f respectively).

Barcoated PbI_2

Arrived at the conclusion that the washing processes and the double step MAI deposition are very beneficial for the perovskite films final morphology, both procedures were made starting from a layer of printed PbI_2. The PbI_2 layer was deposited via barcoating (as described in sections 2.9.1 and 3.1.1) using a PbI_2 400 mg/ml solution and the gas quenching. A Dyesol MAI was used. The concentration for the first step selected was 4 mg/ml and for the second one 40 mg/ml. After the MAI depositions, an IPA cleaning was done. Having used the Dyesol MAI, the perovskite film results to be blurred and reach of impurities even though in some areas the perovskite crystals are really defined (due to the double MAI step) (fig. 3.9a). After the IPA cleaning (fig. 3.9b), the halos disappear and the impurities are minimized.

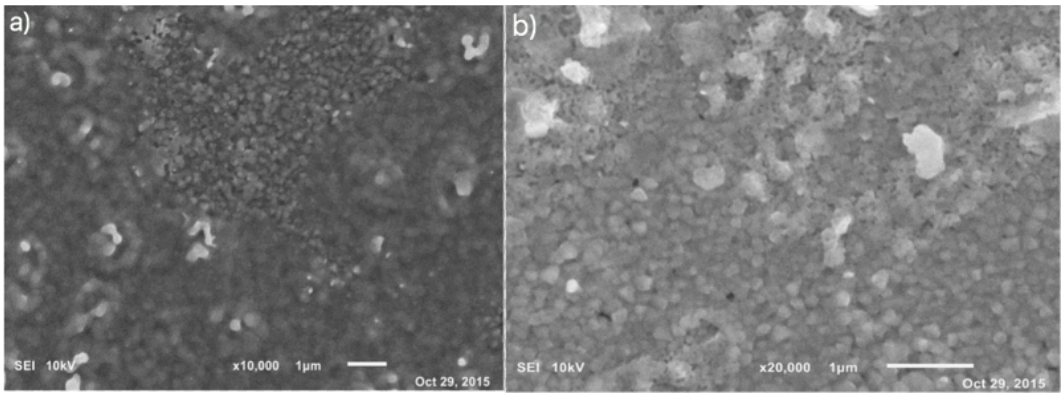

Figure 4.9 SEM images of a perovskite film with barcoated PbI2 layer a) before and b)after IPA cleaning, respectively.

4.3 Crystalline structure : XRD spectra

X-ray diffraction spectra provide information about the chemical composition of the perovskite film. The most important peaks which can be observed from the plots are reported in table 5.3.

Peak Position	Compound	Plane
12.7°	PbI_2	
14.06°	$CH_3NH_3PbI_3$	(110)
20°	$CH_3NH_3PbI_3$	(112)
24.5°	$CH_3NH_3PbI_3$	(121)
28.4°	$CH_3NH_3PbI_3$	(220)
30.1°	ITO-Pedot Substarte	
31.8°	$CH_3NH_3PbI_3$	(114)

Table 4.4 Different peaks expected in the XRD spectrum of CH3NH3PbI3 deposited on the top of FTO.

In order to evaluate the impact of the double step MAI deposition, ratios between the areas under the peaks associated to the different crystallographic planes are considered. In this way we define the relative change in the direction of growth of perovskite crystals. XRD is also useful in order to find different materials, such as residual precursors, PbI_2 or MAI, chemical species formed from degradation of perovskite, hydrated forms. The MAI steps and the consequent measurements

were done on both spinned (fig. 4.10) and barcoated (fig. 4.11) PbI_2 layer to evaluate the effects of the two different PbI_2 morphology. The (16+40) mg/ml and (10+40) mg/ml double MAI steps are analysed. The same perovskite peaks are observed, which proves that the barcoated PbI_2 layer does not cause the growth along new different crystallographic planes. Furthermore the same trend between the two different double steps is observed: in the (16+40) mg/ml double step the peaks are more pronounced both with the spinned and the barcoated PbI_2. Non reacted Lead Iodide peaks are not found in the XRD spectrum of the spincoated PbI_2 layer, while a shoulder is observed in all the spectra of the PbI_2 barcoated case. Probably the too rich in pinholes morphology did not allow the MAI to penetrate deep. In the Barcoated case, a comparison with a single MAI step was done. From figure 4.12 it can be noted that the perovskite peak increases with the use of the double step MAI deposition. In addition to that the unreacted Lead Iodide corresponding peak greatly decreases.

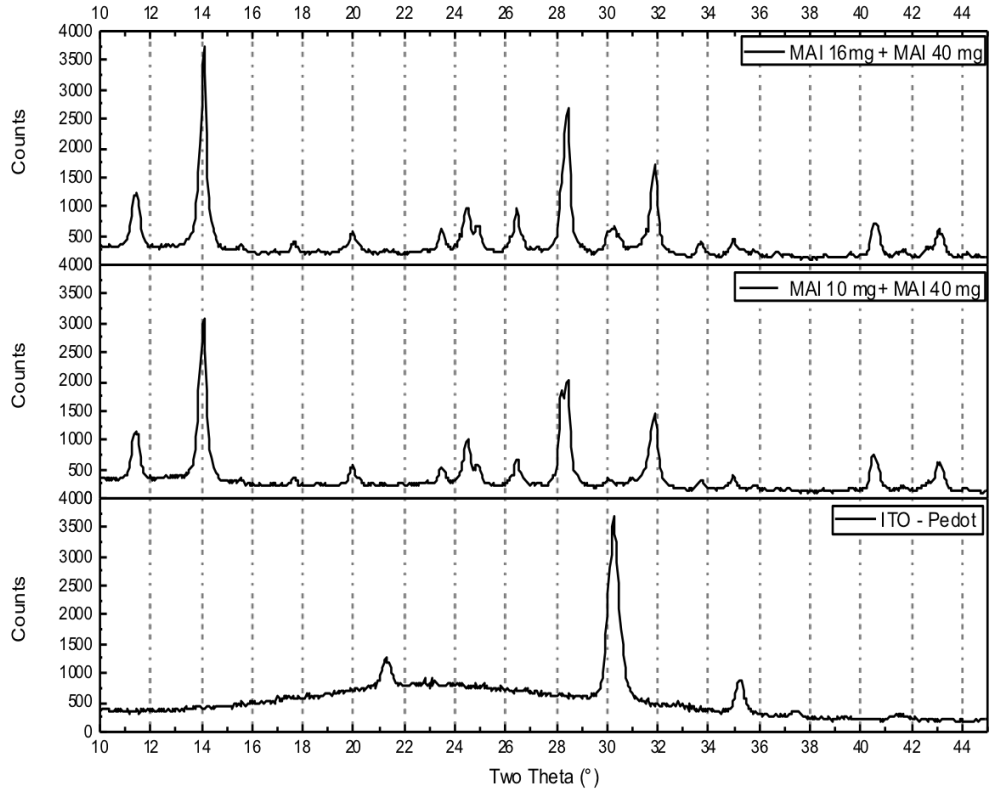

Figure 4.10 X-ray diffraction spectrum of perovskite thin film obtained from different double step MAI depositions on a spinned PbI2 layer.

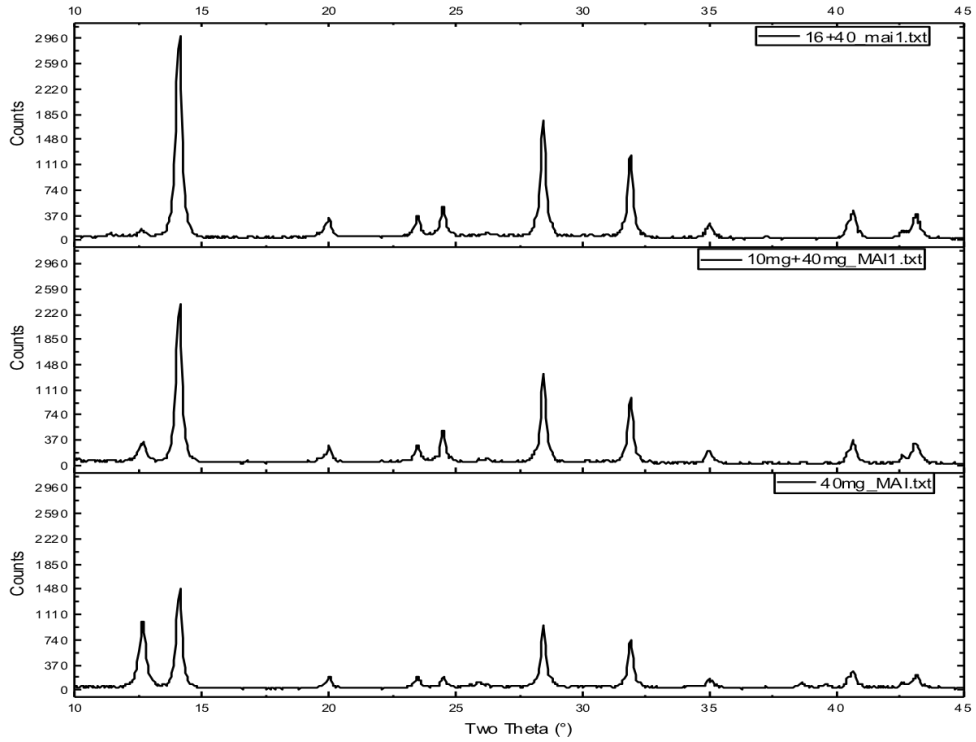

Figure 4.11 X-ray diffraction spectrum of perovskite thin film obtained from different double step MAI depositions on a barcoated PbI2 layer.

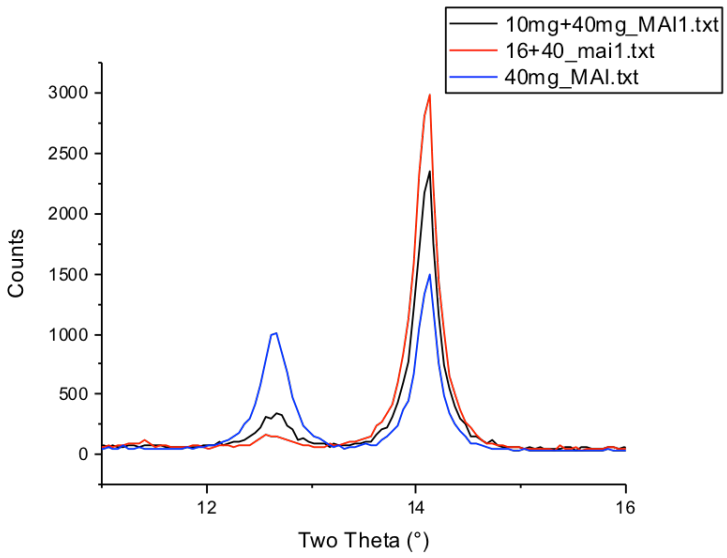

Figure 4.12 X-ray diffraction spectrum of perovskite thin film obtained from different double step MAI depositions on a barcoated PbI2 layer.

Chapter 5

Devices

The optimization of the perovskite morphology has been used to select the most promising deposition conditions for the realization of complete solar cells. The electrical characterization of complete devices is presented in this chapter.
All the devices prepared are characterized by a planar inverted architecture (described in section 2.4.1). The greatest variation between them is the different deposition method of the perovskite layer. The chapter is divided into two sections: the first one concerning totally spincoating devices, the second one in which the perovskite layer is partially (in the two-step deposition) or entirely (in the one-step deposition) deposited through barcoating. The attention will be focused on the different arguments analysed in the previous chapter and on the fabrication of partially printed devices.

5.1 Spincoating

The advantages of spin coating are the simplicity and relative ease with which a process can be set up coupled with the thin and uniform coating that can be achieved. Due to the ability to have high spin speeds the high airflow leads to fast

drying times. On the other hand, the disadvantage of this technique is that it is an inherently batch (single substrate) process and therefore relatively low throughput compared to roll-to-roll processes. Finally, the material usage is typically very low at around 10% or less with the rest being flung off the side and wasted. In this section the perovskite layer is completely deposited by spincoating to see what are the effects of the morphological studies described in the previous chapter.

5.1.1 Effects of IPA cleaning

For the first set of devices, the different PbI_2 thicknesses obtained from the section 4.1.1 study were used. The only two parameters that vary are the PbI_2 thickness and the presence or not of the IPA cleaning. The MAI layer is kept constant to highlight only the effects of the other two factors: a double synthetized MAI step deposition via spincoating was used (10 mg/ml for the first step and 40 mg/ml for the second one). The spincoating parameters are maintained constant (2000 rpm, 2000 acc, 35 sec). The PCBM and the AZO layers are deposited again via spincoating as described in section 3.2.3: 2000 rpm, 2000 acc, 50 sec in both cases.

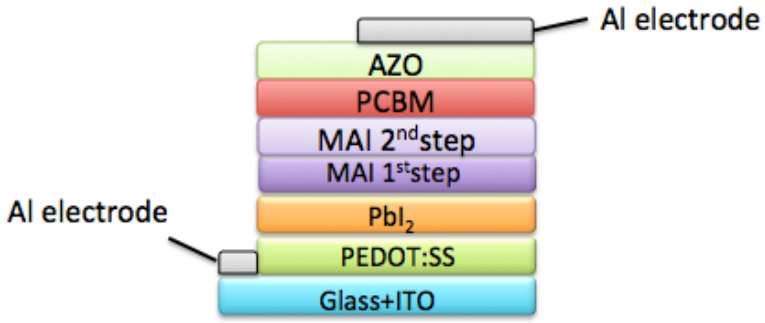

Figure 5.1 Device structure

Devices	PbI_2			IPA cleaning
	Concentration (mg/ml)	rpm, acc.	Thickness (nm)	
1	200	2000, 2000	178	yes
2	//	//	//	no
4	300	4000, 4000	195	yes
5	//	//	//	no

Table 5.1 First set devices parameters.

In all the J-V and dark curves, the solid lines represent the direct scan, while the empty lines represent the reverse scan (in each graph). In the legend the first number refers to the device number, the second one refers to the pixel number, “Light” or “Dark” explains the measurement condition and “F” or “R” refers to a direct scan or a reverse one, respectively.

From the obtained performance (table 5.1) it can be noted that the final efficiency of the device strongly depends on the IPA cleaning. In the case in which the PbI_2 thickness is about 178 nm, the efficiency increases from 1.38% (device 2 without IPA cleaning) to 4.33% (device 1 with IPA cleaning). The same trend can be noticed also with the other two devices: from a 1.38% efficiency without IPA cleaning (device 5) to a 3.53% of efficiency with IPA cleaning (device 4). Thus the IPA cleaning turns out to be crucial If residuals are left on the layer: the perovskite surface residues are partially removed, thus the layer is more homogeneous and suitable for the deposition of subsequent layers. The defects density at the perovskite surface decreases and therefore also the number of traps. In the J-V curves (especially for the devices 2 and 5, those without IPA cleaning) it can be noted that the significant power losses is caused by the presence of a shunt resistance (R_{SH}), that leads to a remarkable lowering of the curve. This type of resistance is generally due to manufacturing defects, rather than solar cell design. It can be said that the performance of this set of devices are greatly affected by the presence of defects, which can be partially removed with the addition of the IPA cleaning step.

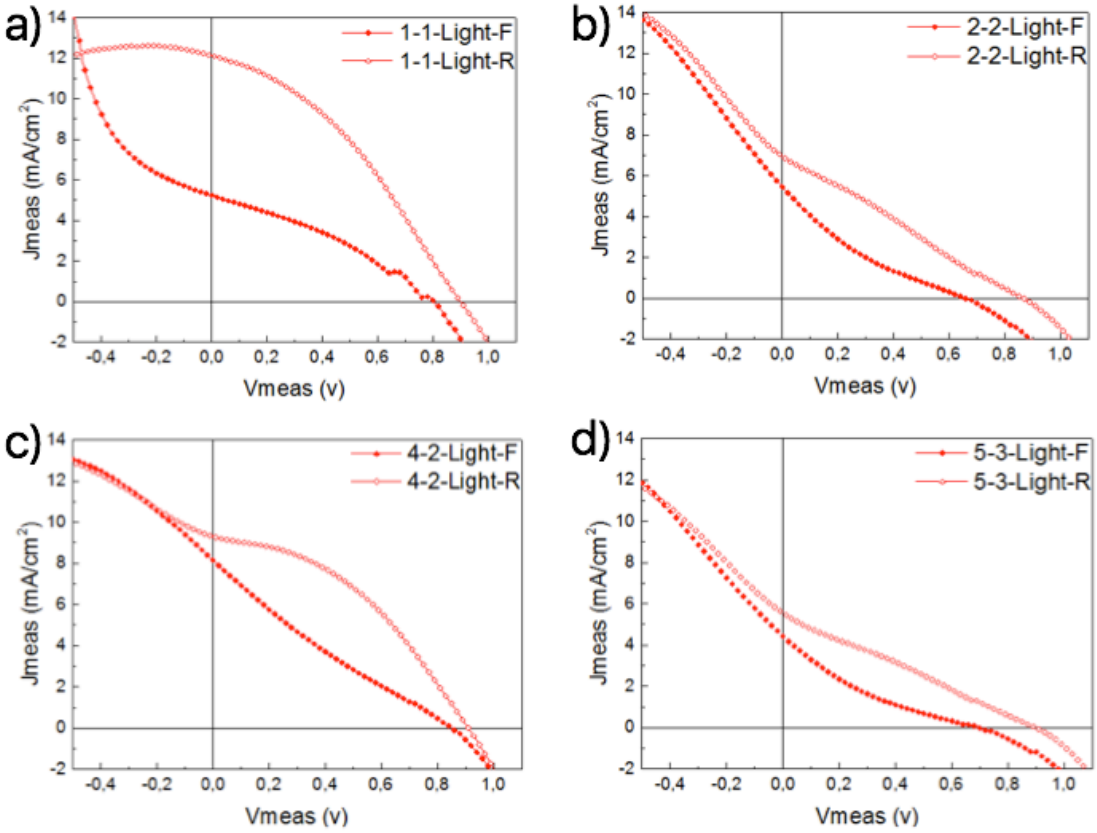

Figure 5.2 J-V Characteristic of a)device 1, b)device 2, c)device 4, d)device 5.

Device	V_{oc} (V)	J_{sc} (mA/cm^2)	Fill Factor (%)	Efficiency (%)
1	0.95	12.0	38.2	4.33
2	0.85	6.2	26.3	1.38
4	0.92	9.7	39.4	3.53
5	0.90	6.0	25.3	1.38

Table 5.2 Main parameters (Voc, Jsc, FF and efficiency) obtained from the analysis of figure 5.1

5.1.2 Effects of consecutive measurements

All the devices investigated in this study present hysteresis (as it can be seen from all the J-V curves). Taking as an example the device 1 of the first set (of which the parameters are described in table 5.1), it has been noted that by repeating the measurement on the same pixel, the hysteresis decreases. In particular six different consecutive scans were made (fig. 5.3). In the first scan the hysteresis is very strong (red lines), but after few scans a reduction is observed. Until the third scan the hysteresis decreases, while up to the sixth scan the device starts to degrade (green lines). The origin of this behaviour is not yet fully known, as indeed the origin of the hysteresis itself. As mentioned before, the hysteresis origin could be due to the presence of traps. Lower the quality of the perovskite, greater the hysteresis phenomenon. The results indicate that the different and consecutive scans can passivate the trap states. This variation of hysteresis is therefore due to a movement of ions.

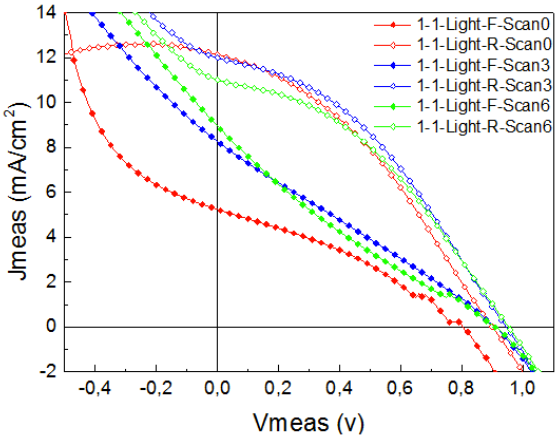

Figure 5.3 Variation of the J-V characteristic of the same device (number 1, first set) due to the increasing number of measurements.

5.1.3 Effects of different double step MAI depositions

The best device of the previous batch has been used as a reference for the optimization of the MAI deposition. For this second set, the devices are prepared using the double step MAI deposition method studied and described in section

4.2.3. The synthetized MAI is used and the spincoating parameters used were 2000 rpm, 2000 acc for 35 seconds.The PbI_2 layer (spincoated at 2000 rpm, 2000 acc, 35 sec, about 300 nm) is kept constant to see the variations due to the different MAI steps. The PCBM and the AZO layers are deposited again via spincoating as described in section 3.2.3: 2000 rpm, 2000 acc, 50 sec in both cases.

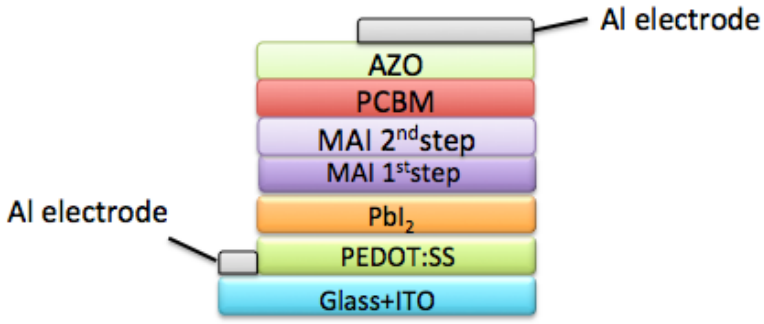

Figure 5.4 Device structure

The different parameters of each device are presented in table 5.3. The second MAI deposition step is maintained constant. The resulting performances (reported in table 5.4) follow a clear trend: lower the first step MAI concentration, greater the efficiency. A 2.81% of efficiency is obtained with a 4 mg/ml first step concentration, 2.43% for 10mg/ml and 1.80% for 16 mg/ml. Comparing the performance with the SEM images of the corresponding morphology (fig. 5.4), it can be noted that the greater surface homogeneity leads to better results. The perovskite layer obtained with the double step MAI deposition (4+40) mg/ml is more homogeneous and presents no surface patterns. In the figure 5.4 f), there are some crowns that may not allow the perfect successive layers deposition. The J-V curves (fig. 5.4) do not exhibit a perfect trend: the lost in performances is caused by the presence of a high shunt resistance due to an high defect density. Despite all, from a morphological point of view, without considering only the performances, the best layer seems to be the one obtained using a 10 mg/ml first step (device 3) because the grater perovskite grains. Furthermore the parameters values do not differ from the device which presents the best efficiency (table 5.4). Thus the double step MAI deposition (10+40) mg/ml leads to good perovskite morphology and it can be positively evaluated and translated

in the two-step fabrication of the partially printed devices that will be analysed in the next section.

Device	MAI	
	1st step concentration (mg/ml)	2nd step concentration (mg/ml)
1	4	40
3	10	40
5	16	40

Table 5.3 Second set devices parameters.

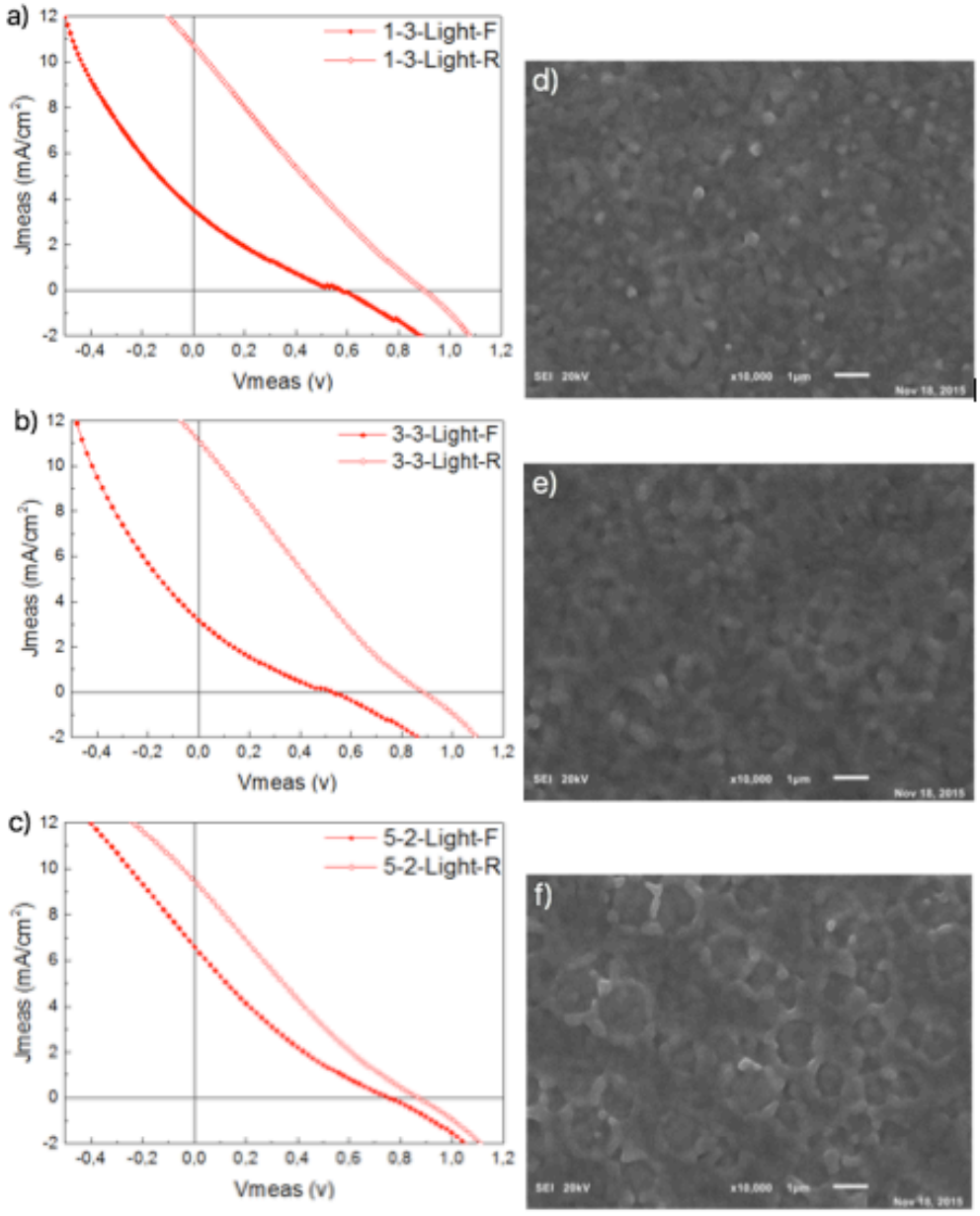

Figure 5.5 J-V characteristics of a)device 1, b)device 3, c)device 4 and corresponding perovskite morphology (d, e, f, respectively).

Device	V_{oc} (V)	J_{sc} (mA/cm^2)	Fill Factor (%)	Efficiency (%)
1	0.92	13.5	22.6	2.81
3	0.89	12.2	22.6	2.43
5	0.88	9.8	20.9	1.80

Table 5.4 Main parameters (Voc, Jsc, FF and efficiency) obtained from the analysis of figure 5.5.

5.2 Barcoating

The aim of this thesis is to translate the optimization of the perovskite morphology from a lab-scale process to a large-scale production, which will preferably include a cost-competitive roll-to-roll printing production. The morphology optimization described in Chapter 4 is used for the fabrication of partially printed perovskite solar cells. Two different sets of devices were made using the two different deposition methods: two-steps and one-step. Despite the non optimal deposition conditions (no humidity and temperature control, partially and not total quenching control), discrete performances were obtained.

5.2.1 Two-step deposition

In the third set the aim is to find out if the morphology obtained by the barcoater technique can lead to working devices. For these two devices, the MAI layer (double step, 10mg/ml+40 mg/ml, both spincoated at 2000 rpm, 2000 acc, for 35 seconds), the barcoater parameters (high of the bar, speed) and the type of gas quenching for the PbI_2 drying are kept constant. The bar high is set at the 20 nm corresponding value on the barcoater scale and the speed was set at 50 mm/s. The PCBM and the AZO layers are deposited again via spincoating as described in section 3.2.3: 2000 rpm, 2000 acc, 50 sec in both cases.

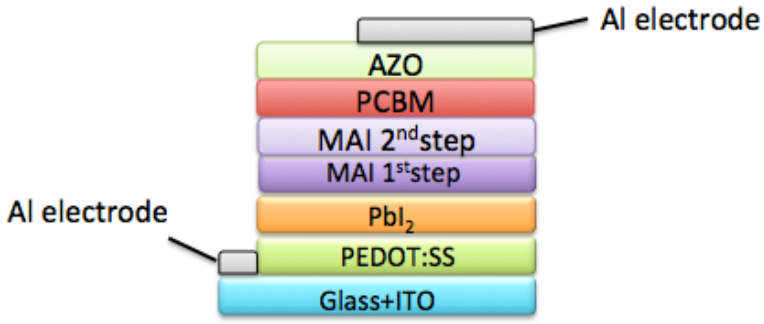

Figure 5.6 Device structure

From the data reported in the table 5.5 it can be noted that the PbI_2 thickness obtained with the barcoating technique varies greatly along the substrate. This could be a problem for the MAI penetration and thus the perovskite formation. From the analysis of the main parameters, the efficiencies obtained are similar (1.26% for device 5 and 1.20% for device 6). The parameter that varies greatly between the two cases is the current density J_{sc}: 7.0 mA/cm^2 for the device 5 and 1.1 mA/cm^2 for the other one. In both cases the PbI_2 layer morphology (fig. 5.6c) did not help in the reaction with the MAI and in the extraction of the charge. The presence of pinholes does not lead the MAI molecules to penetrate deep in the PbI_2. Thus some lead iodide remains unreacted and blocks the transport of charges to the electrodes. Despite the low performances, the devices are still functioning. This is a very positive result considering the simplicity of the method of deposition and uncontrollable working conditions (all the devices have been printed in air without humidity control). To improve the devices performances, the PbI_2 morphology has to be optimized: the aim is to obtain a smooth and almost pinhole-free layer.

Device	**PbI_2**	
	Concentration (mg/ml)	**Thickness (nm)**
5	400	200-500
6	400	300-440

Table 5.5 Third set device parameters.

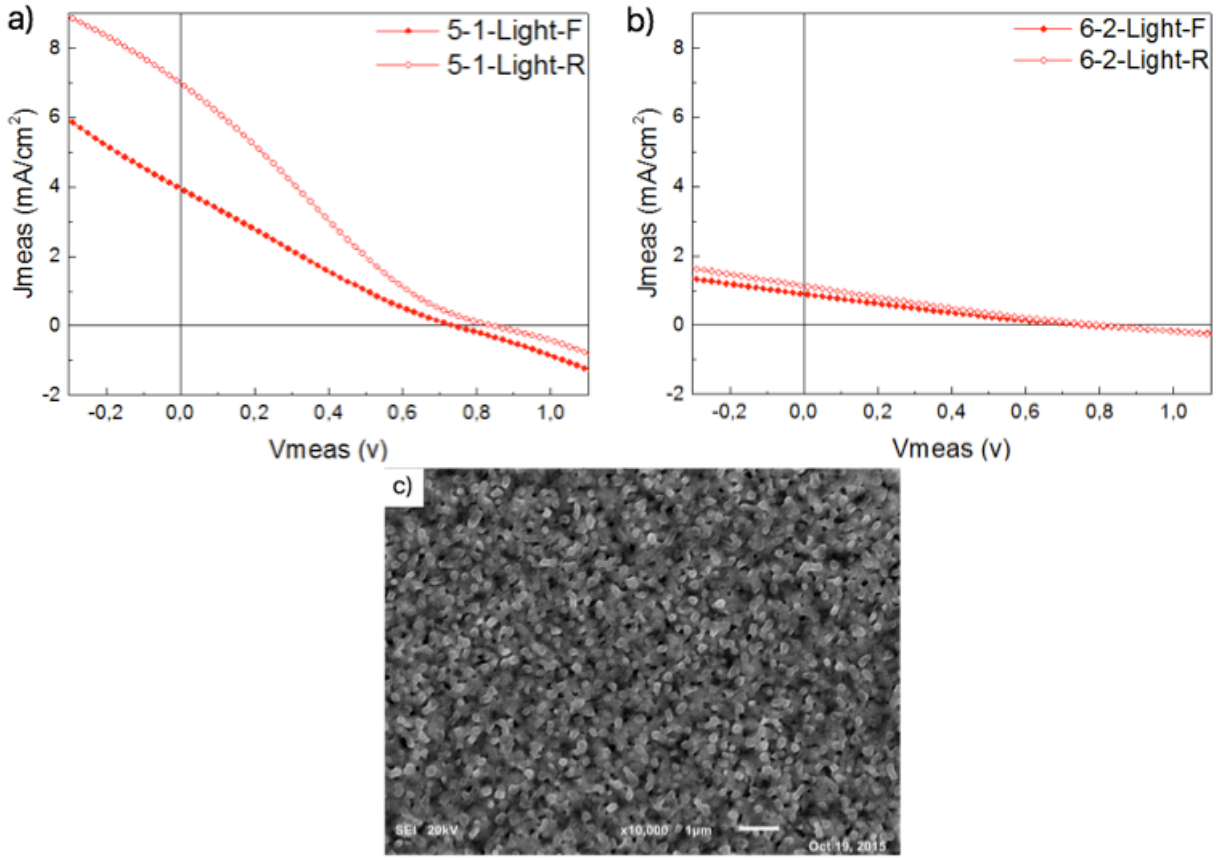

Figure 5.7 J-V characteristics of devices a)5 and b)6. Below (c), the typical PbI2 morphology printed using the barcoating and the gas quenching techniques.

Device	V_{oc} (V)	J_{sc} (mA/cm^2)	Fill Factor (%)	Efficiency (%)
5	0.84	7.0	21.3	1.26
6	0.80	1.1	21.7	1.20

Table 5.6 Main parameters (Voc, Jsc, FF and efficiency) obtained from the analysis of figure 5.6

5.2.2 One-step deposition

In the fourth and final set of devices, the one-step deposition method is used to print the perovskite layer using the barcoating technique. With this method the perovskite layer is printed with a single deposition. The final morphology of the perovskite is much less controllable, but the matching problem between the morphology of the printed PbI_2 and the spinned MAI found in the previous set does no longer exist.

The same precursor solution was used for all the devices. The bar high (20 nm on the barcoater scale) and the speed value (50 mm/s) are maintained constant. The only parameter that varied is the annealing condition of the layer. In this experiment all the four annealing methods described in section 3.2.3 are used. The PCBM and the AZO layers are deposited again via spincoating as described in section 3.2.3: 2000 rpm, 2000 acc, 50 sec in both cases.

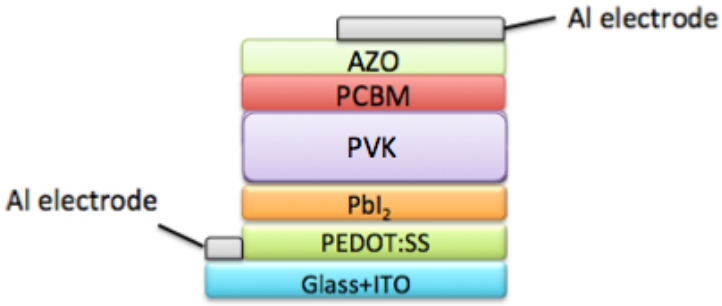

Figure 5.8 Device structure

The device performances are highly dependent on the processing conditions. With a total air annealing (devices 1 and 2) efficiencies from 2.44% to 3.39% are obtained, while with a partial annealing in air followed by a partial annealing in glovebox (where the nitrogen atmosphere is completely controlled) efficiencies from 3.56% to 3.78% are obtained (devices 3 and 4). Adding an annealing step in the air but under a nitrogen hood, the efficiency rise up to 4.65% (device 5). The J-V curves (fig. 5.9) present a good shape and in the best case (device 5, light blue lines) it can be noted that the hysteresis is almost zero. This turns out to be a very positive result because the perovskite layer was entirely printed in non controllable conditions and with a very simple printing method.

Sample	Annealing
1	30 min @T_{amb} in air + 90 min @90°C in air
2	20 min @T_{amb} in N_2 atmosphere + 90 min @90°C in air
3	30 min @T_{amb} in air + 30 min @90°C in air + 30 min @90°C in GB
4	30 min @T_{amb} in air + 30 min @90°C in air + 30 min @90°C in GB
5	20 min @T_{amb} in N_2 atmosphere + 30 min @90°C in air + 60 min @90°C in GB
6	20 min @T_{amb} in N_2 atmosphere + 30 min @90°C in air + 60 min @90°C in GB

Table 5.7 Fourth set device parameters.

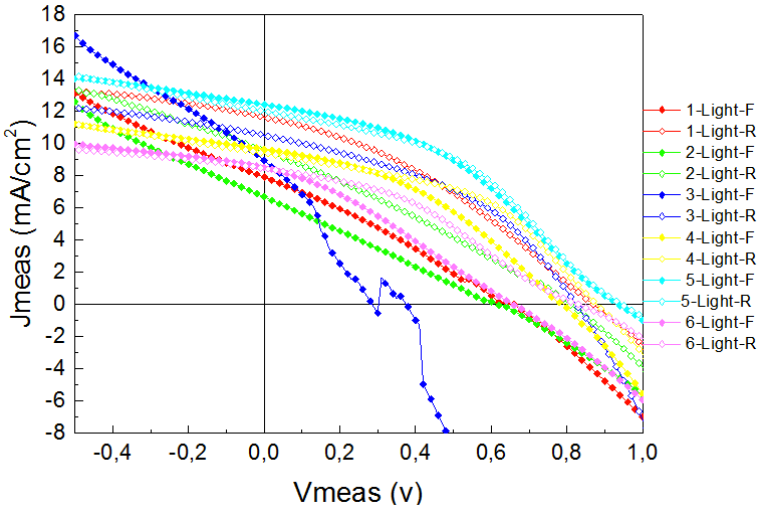

Figure 5.9 J-V characteristics of all the devices.

Device	V_{oc} (V)	J_{sc} (mA/cm^2)	Fill Factor (%)	Efficiency (%)
1	0.86	11.5	34.2	3.39
2	0.83	10.5	28.0	2.44
3	0.79	10.6	42.9	3.56
4	0.88	9.4	45.9	3.78
5	0.94	12.0	41.0	4.65
6	0.83	8.5	35.9	2.52

Table 5.8 Main parameters (Voc, Jsc, FF and efficiency) obtained from the analysis of figure 5.7

Conclusions

The performance of perovskite solar cells is deeply influenced by the quality of the perovskite film, suggesting that the optimization of film formation and crystallization is of paramount importance especially for the fabrication of printed devices. The classical spincoating technique has been used for the optimizations steps and as a reference for the films morphology obtained with the barcoating scalable process. For the first time the barcoating technique was introduced in the perovskite-based solar cells fabrication. An optimization of the perovskite morphology obtained through two-step deposition method was done. The different lead iodide film morphologies deposited by spincoating or barcoating were compared. Pure Dyesol MAI is not the best choice as perovskite precursor, since better morphology can be achieved by using synthesized MAI. The double step MAI deposition method was introduced to increase the MAI penetration level on the lead iodide layer and to better control the perovskite grain crystallinity and growth. IPA cleaning turns out to be crucial if residuals are left on the perovskite layer: the surface defects density decreases. The devices with the PbI_2 barcoated layer show efficiency between 1.20% and 1.26%. The devices in which the perovskite layer was barcoated through a one-deposition method, show better efficiencies (from 2.44% to 4.65%). With the one-step deposition the partial conversion problem is avoided. Despite the low performances, the devices are still functioning. This is a very positive result considering the simplicity of the method of deposition and the uncontrollable working conditions (all the devices have been printed in air without humidity control). The feasibility of partially barcoated perovskite-based solar cells has been validated in this work; further improvements are still required for the achievement of fully printable devices: the

deposition method of the other layer should be optimized and the top and bottom electrodes should be solution processed. Furthermore the atmospheric conditions control is another primary aim: the devices fabrication under constant conditions is crucial for a large-scale production.

Bibliography

[1] Kojima, K. Teshima, Y. Shirai, and T. Miyasaka, “Organometal halide perovskites as visible-light sensitizers for photovoltaic cells,” Journal of the American Chemical Society, vol. 131, no. 17, pp. 6050–6051, 2009.

[2] N.-G. Park, “Perovskite solar cells: an emerging photovoltaic technology,” Materials Today, vol. 18, no. 2, pp. 65–72, 2015.

[3] M. A. Green, A. Ho-Baillie, and H. J. Snaith, “The emergence of perovskite solar cells,” Nature Photonics, vol. 8, no. 7, pp. 506–514, 2014.

[4] T. C. Sum and N. Mathews, “Advancements in perovskite solar cells: photophysics behind the photovoltaics,” Energy & Environmental Science, vol. 7, no. 8, pp. 2518–2534, 2014.

[5] C. Li, X. Lu, W. Ding, L. Feng, Y. Gao, and Z. Guo, “Formability of abx3 (x= f, cl, br, i) halide perovskites,” Acta Crystallographica Section B: Structural Science, vol. 64, no. 6, pp. 702–707, 2008.

[6] T. Umebayashi, K. Asai, T. Kondo, and A. Nakao, “Electronic structures of lead iodide based low-dimensional crystals,” Physical Review B, vol. 67, no. 15, p. 155405, 2003.

[7] P. Gao, M. Graetzel, and M. K. Nazeeruddin, “Organohalide lead perovskites for photo- voltaic applications,” Energy & Environmental Science, vol. 7, no. 8, pp. 2448–2463, 2014.

[8] J. L. Knutson, J. D. Martin, and D. B. Mitzi, “Tuning the band gap in hybrid tin iodide perovskite semiconductors using structural templating,” Inorganic chemistry, vol. 44, no. 13, pp. 4699–4705, 2005.

[9] M. Jansen and H. Letschert, “Inorganic yellow-red pigments without toxic metals,” Nature, vol. 404, no. 6781, pp. 980–982, 2000.

[10] I.Borriello, G. Cantele, and D. Ninno, “Ab initio investigation of hybrid organic-inorganic perovskites based on tin halides,” Physical Review B, vol. 77, no. 23, p. 235214, 2008.

[11] N. K. Noel, S. D. Stranks, A. Abate, C. Wehrenfennig, S. Guarnera, A.-A. Haghighirad, A. Sadhanala, G. E. Eperon, S. K. Pathak, M. B. Johnston, et al., “Lead-free organic– inorganic tin halide perovskites for photovoltaic applications,” Energy & Environmental Science, vol. 7, no. 9, pp. 3061–3068, 2014.

[12] Y. Ogomi, A. Morita, S. Tsukamoto, T. Saitho, N. Fujikawa, Q. Shen, T. Toyoda, K. Yoshino, S. S. Pandey, T. Ma, et al., “Ch3nh3sn x pb (1–x) i3 perovskite solar cells covering up to 1060 nm,” The Journal of Physical Chemistry Letters, vol. 5, no. 6, pp. 1004– 1011, 2014.

[13] D. Mitzi and C. Kagan, “Organic-inorganic hybrid materials as semiconducting channels in thin-film field-effect transistors,” Science, vol. 286, no. 5441, pp. 945–947, 1999.

[14] K. T. Butler, J. M. Frost, and A. Walsh, “Band alignment of the hybrid halide perovskites ch 3 nh 3 pbcl 3, ch 3 nh 3 pbbr 3 and ch 3 nh 3 pbi 3,” Materials Horizons, vol. 2, no. 2, pp. 228–231, 2015.

[15] E. Kozma and M. Catellani, “Perylene diimides based materials for organic solar cells,” Dyes and Pigments, vol. 98, no. 1, pp. 160–179, 2013.

[16] N. Kitazawa, Y. Watanabe, and Y. Nakamura, “Optical properties of ch3nh3pbx3 (x= halo- gen) and their mixed-halide crystals,” Journal of materials science, vol. 37, no. 17, pp. 3585– 3587, 2002.

[17] H. J. Snaith, A. Abate, J. M. Ball, G. E. Eperon, T. Leijtens, N. K. Noel, S. D. Stranks, J. T.-W. Wang, K. Wojciechowski, and W. Zhang, “Anomalous hysteresis in perovskite solar cells,” The Journal of Physical Chemistry Letters, vol. 5, no. 9, pp. 1511–1515, 2014.

[18] Y. Shao, Z. Xiao, C. Bi, Y. Yuan, and J. Huang, “Origin and elimination of photocurrent hysteresis by fullerene passivation in ch3nh3pbi3 planar heterojunction solar cells,” Nature communications, vol. 5, 2014.

[19] J.-H. Im, H.-S. Kim, and N.-G. Park, “Morphology-photovoltaic property correlation in perovskite solar cells: One-step versus two-step deposition of ch3nh3pbi3,” Apl Materials, vol. 2, no. 8, p. 081510, 2014.

[20] J. Burschka, N. Pellet, S.-J. Moon, R. Humphry-Baker, P. Gao, M. K. Nazeeruddin, and M. Graetzel, “Sequential deposition as a route to high-performance perovskite-sensitized solar cells,” Nature, vol. 499, no. 7458, pp. 316–319, 2013.

[21] P. Beckmann, “Correction: A review of polytypism in lead iodide,” Crystal Research and Technology, vol. 45, no. 5, 2010.

[22] G. Gurina and K. Savchenko, “Intercalation and formation of complexes in the system of lead (ii) iodide–ammonia,” Journal of Solid State Chemistry, vol. 177, no. 3, pp. 909–915, 2004.

[23] Salau, “Fundamental absorption edge in pbi 2: Ki alloys,” Solar Energy Materials, vol. 2, no. 3, pp. 327–332, 1980.

[24] M. Liu, M. B. Johnston, and H. J. Snaith, “Efficient planar heterojunction perovskite solar cells by vapour deposition,” Nature, vol. 501, no. 7467, pp. 395–398, 2013.

[25] Q. Chen, H. Zhou, Z. Hong, S. Luo, H.-S. Duan, H.-H. Wang, Y. Liu, G. Li, and Y. Yang, “Planar heterojunction perovskite solar cells via vapor-assisted solution process,” Journal of the American Chemical Society, vol. 136, no. 2, pp. 622–625, 2013.

[26] M. A. Green, A. Ho-Baillie, H. J. Snaith, Nat. Photonics 2014, 8, 506.

[27] N. Espinosa, L. Serrano-luján, A. Urbina, F. C. Krebs, Sol. Energy Mater. Sol. Cells 2015, 137, 303.

[28] Z. Wei, H. Chen, K. Yan, S. Yang, Angew. Chem. 2014, 126, 13455.

[29] F. C. Krebs, Sol. Energy Mater. Sol. Cells 2009, 93, 394.

[30] T. R. Andersen, H. F. Dam, M. Hösel, M. Helgesen, J. E. Carlé, T. T. Larsen-Olsen, S. A. Gevorgyan, J. W. Andreasen, J. Adams, N. Li, F. Machui, G. D. Spyropoulos, T. Ameri, N. Lemaître, M. Legros, A. Scheel, D. Gaiser, K. Kreul, S. Berny, O. R. Lozman, S. Nordman, M.

Välimäki, M. Vilkman, R. R. Søndergaard, M. Jørgensen, C. J. Brabec, F. C. Krebs, Energy Environ. Sci. 2014, 7, 2925.

[31] T. Barrows, A. J. Pearson, C. K. Kwak, A. D. Dunbar, A. R. Buckley, D. G. Lidzey, Energy Environ. Sci. 2014, 7, 2944.

[32] R. R. Søndergaard, M. Hösel, F. C. Krebs, J. Polym. Sci., Part B: Polym. Phys. 2013, 51, 16.

[33] S. Hong, M. Yi, H. Kang, J. Kong, W. Lee, J.-R. Kim, K. Lee, Sol. Energy Mater. Sol. Cells 2014, 126, 107.

[34] M. Schrödner, S. Sensfuss, H. Schache, K. Schultheis, T. Welzel, K. Heinemann, R. Milker, J. Marten, L. Blankenburg, Sol. Energy Mater. Sol. Cells 2012, 107, 283.

[35] K. Hwang, Y. Jung, Y. Heo, F. H. Scholes, S. E. Watkins, J. Subbiah, D. J. Jones, D. Kim and D. Vak, “Toward Large Scale Roll-to-Roll Production of Fully Printed Perovskite Solar Cells”, Journal of the Advanced Energy Materials, Jenuary 7, 2015, 27, 1241–1247

[36] S. Sun, T. Salim, N. Mathews, M. Duchamp, C. Boothroyd, G. Xing, T. C. Sum and Y. M. Lam, Energy Environ. Sci., 2014, 7, 399–407.

[37] J.-Y. Jeng, Y.-F. Chiang, M.-H. Lee, S.-R. Peng, T.-F. Guo, P. Chen and T.-C. Wen, Adv. Mater., 2013, 25, 3727–3732.

[38] N.J.Jeon,J.H.Noh,Y.C.Kim,W.S.Yang,S.Ryuand, S. I. Seok, Nat. Mater., 2014, 13, 897–903.

[39] H.-S. Kim and N.-G. Park, J. Phys. Chem. Lett., 2014, 5, 2927– 2934.

[40] H. J. Snaith, A. Abate, J. M. Ball, G. E. Eperon, T. Leijtens, N. K. Noel, S. D. Stranks, J. T.-W. Wang, K. Wojciechowski and W. Zhang, J. Phys. Chem. Lett., 2014, 5, 1511–1515.

[41] E. L. Unger, E. T. Hoke, C. D. Bailie, W. H. Nguyen, A. R. Bowring, T. Heumuller, M. G. Christoforo and M. D. McGehee, Energy Environ. Sci., 2014, 7, 3690–3698.

[42] Z. Xiao, C. Bi, Y. Shao, Q. Dong, Q. Wang, Y. Yuan, C. Wang, Y. Gao and J. Huang, Energy Environ. Sci., 2014, 7, 2619– 2623.

[43] J. Even, L. Pedesseau and C. Katan, J. Phys. Chem. C, 2014, 118, 11566–11572.

[44] S. N. Habisreutinger, T. Leijtens, G. E. Eperon, S. D. Stranks, R. J. Nicholas and H. J. Snaith, Nano Lett., 2014, 14, 5561– 5568.

[45] W. Yan, Y. Li, W. Sun, H. Peng, S. Ye, Z. Liu, Z. Bian and C. Huang, RSC Adv., 2014, 4, 33039–33046.

[46] L. E. Polander, P. Pahner, M. Schwarze, M. Saalfrank, 743. C. Koerner and K. Leo, APL Mater., 2014, 2, 081503.

[47] Z. Wu, S. Bai, J. Xiang, Z. Yuan, Y. Yang, W. Cui, X. Gao, Z. Liu, Y. Jin and B. Sun, Nanoscale, 2014, 6, 10505–10510.

[48] P. Docampo, J. M. Ball, M. Darwich, G. E. Eperon and H. J. Snaith, Nat. Commun., 2013, 4.

[49] Z. Zhu, Y. Bai, T. Zhang, Z. Liu, X. Long, Z. Wei, Z. Wang, L. Zhang, J. Wang, F. Yan and S. Yang, Angew. Chem., Int. Ed., 2014, 53, 12571–12575.

[50] A. S. Subbiah, A. Halder, S. Ghosh, N. Mahuli, G. Hodes and S. K. Sarkar, J. Phys. Chem. Lett., 2014, 5, 1748–1753.

[51] Y.-Y. Yu, R.-S. Chiang, H.-L. Hsu, C.-C. Yang and C.-P. Chen, Nanoscale, 2014, 6, 11403–11410.

[52] C.-W. Chen, H.-W. Kang, S.-Y. Hsiao, P.-F. Yang, K.-M. Chiang and H.-W. Lin, Adv. Mater., 2014, 26, 6647– 6652.

[53] A. T. Barrows, A. J. Pearson, C. K. Kwak, A. D. F. Dunbar, A. R. Buckley and D. G. Lidzey, Energy Environ. Sci., 2014, 7, 2944–2950.

[54] J. Seo, S. Park, Y. Chan Kim, N. J. Jeon, J. H. Noh, S. C. Yoon and S. I. Seok, Energy Environ. Sci., 2014, 7, 2642–2646.

[55] P.-W. Liang, C.-Y. Liao, C.-C. Chueh, F. Zuo, S. T. Williams, X.-K. Xin, J. Lin and A. K. Y. Jen, Adv. Mater., 2014, 26, 3748–3754.

[56] Q. Wang, Y. Shao, Q. Dong, Z. Xiao, Y. Yuan and J. Huang, Energy Environ. Sci., 2014, 7, 2359–2365.

[57] Tadatsugu Minami. Transparent conducting oxide semiconductors for transparent electrodes. 2005. doi: 10.1088/0268-1242/20/4/004.

[58] L. Sims et al. Comprehensive Renewable Energy. Elsevier, 2012, pp. 439– 480. isbn: 9780080878737. doi: 10.1016/B978-0-08-087872-0.00120- 7. url: http://www.sciencedirect.com/science/article/pii/ B9780080878720001207.

[59] Riccardo Po et al. Polymer- and carbon-based electrodes for polymer solar cells: Toward low-cost, continuous fabrication over large area. 2012. doi: 10.1016/j.solmat.2011.12.022.

[60] Diener Femto. url: http://www.plasma.de/pdfs/femto-englisch. pdf.

[61] Wu Z, Chen Z, Du X, Logan JM, Sippel J, Nikolou M, et al. Transparent, conductive carbon nanotube films. Science 2004;305(5688):1273–6.

[62] http://www.ossila.com/pages/perovskites-and-perovskite-solar-cells-an-introduction

[63] http://plasticphotovoltaics.org/lc/lc-fabrication/lc-coating/lc-slotdie.html

[64] O. Malinkiewicz, A. Yella, Y. H. Lee, G. M. Espallargas, M. Graetzel, M. K. Nazeeruddin, and H. J. Bolink, “Perovskite solar cells employing organic charge-transport layers,” Nature Photonics, vol. 8, no. 2, pp. 128–132, 2014.

[65] S. D. Stranks, G. E. Eperon, G. Grancini, C. Menelaou, M. J. Alcocer, T. Leijtens, L. M. Herz, A. Petrozza, and H. J. Snaith, “Electron-hole diffusion lengths exceeding 1 micrometer in an organometal trihalide perovskite absorber,” Science, vol. 342, no. 6156, pp. 341–344, 2013.

[66] P. E. Shaw, A. Ruseckas, and I. D. Samuel, “Exciton diffusion measurements in poly (3-hexylthiophene),” Advanced Materials, vol. 20, no. 18, pp. 3516–3520, 2008.

[67] R. R. Lunt, J. B. Benziger, and S. R. Forrest, “Relationship between crystalline order and exciton diffusion length in molecular organic semiconductors,” Advanced Materials, vol. 22, no. 11, pp. 1233–1236, 2010.

[68] D. Zhitomirsky, O. Voznyy, S. Hoogland, and E. H. Sargent, “Measuring charge carrier diffusion in coupled colloidal quantum dot solids,” ACS nano, vol. 7, no. 6, pp. 5282–5290, 2013.

[69] G. Giorgi, J.-I. Fujisawa, H. Segawa, and K. Yamashita, “Small photocarrier effective masses featuring ambipolar transport in methylammonium lead iodide perovskite: A density func- tional analysis,” The Journal of Physical Chemistry Letters, vol. 4, no. 24, pp. 4213–4216, 2013.

[70] C. Wehrenfennig, G. E. Eperon, M. B. Johnston, H. J. Snaith, and L. M. Herz, “High charge carrier mobilities and lifetimes in organolead trihalide perovskites,” Advanced Materials, vol. 26, no. 10, pp. 1584–1589, 2014.

[71] V. I. Klimov, A. Mikhailovsky, D. McBranch, C. Leatherdale, and M. G. Bawendi, “Quan- tization of multiparticle auger rates in semiconductor quantum dots,” Science, vol. 287, no. 5455, pp. 1011–1013, 2000.

[72] G. Xing, N. Mathews, S. S. Lim, N. Yantara, X. Liu, D. Sabba, M. Graetzel, S. Mhaisalkar, and T. C. Sum, “Low-temperature solution-processed wavelength-tunable perovskites for lasing,” Nature materials, vol. 13, no. 5, pp. 476–480, 2014.

[73] Topsöe, H. “Krystallographisch-chemische untersuchungen homologer verbindungen”. *Zeitschri für Kristallographie* **8,** 246–296 (1884).

[74] Even, J., Pedesseau, L., Jancu, J.-M. & Katan, C. Importance of spin-orbit coupling in hybrid organic/inorganic perovskites for photovoltaic applications. *J. Phys. Chem. Lett.* **4,** 2999–3005 (2013).

[75] J. H. Heo, H. J. Han, D. Kim, T. K. Ahn and S. H. Im, “Hysteresis-less inverted $CH_3NH_3PbI_3$ planar perovskite hybrid solar cells with 18.1% power conversion efficiency” , *Energy Environ. Sci.,* 2015, 8, 1602, DOI: 10.1039/c5ee00120j.

[76] Small, Volume 11 Issue 1, pages 10-25, 30 October 2014, DOI: 10.1002/smll.20142767.

[77] Z. Xiao, D. Wang, Q. Dong, Q. Wang, W. Wei, J. Dai, X. Zeng and J. Huang, "Unraveling the hidden function of a stabilizer in a precursor in improving hybrid perovskite film morphology for high efficiency solar cells", *Energy Environ. Sci.,* 2016, 9, 867, DOI: 10.1039/c6ee00183a.

[78] B.-E. Cohen, S. Gamliel, L. Etgar, APL Mater. 2014, 2, 081502.

[79] M. Liu, M. B. Johnston, H. J. Snaith, Nature 2013, 501, 395.

[80] T. M. Schmidt, T. T. Larsen-Olsen, J. E. Carlé, D. Angmo, and F. C. Kreb, "Upscaling of Perovskite Solar Cells: Fully Ambient Roll Processing of Flexible Perovskite Solar Cells with Printed Back Electrodes", Journal of the Advanced Energy Materials, Volume 5, Agoust 2015.

[81] Y. Wu, A. Islam, X. Yang, C. Qin, J. Liu, K. Zhang, W. Peng and L. Han, "Retarding the crystallization of PbI_2 for highly reproducible planar-structured perovskite solar cells via sequential deposition", Energy Environ. Sci., 2014, 7, 2934–2938, DOI: 10.1039/c4ee01624f.

Vorrei ringraziare innanzitutto il Prof. Guglielmo Lanzani per avermi offerto l'opportunità di svolgere la mia tesi di laurea magistrale presso il Center of NanoScience and Technology presso l'Istituto Italiano di Tecnologia. I miei più sinceri ringraziamenti vanno anche al mio correlatore Dott. Mario Caironi per avermi seguita ed aiutata durante tutta l'attività sperimentale, dimostrandomi sempre assoluta disponibilità. Ringrazio inoltre il mio supervisore Carlo Perini senza il quale non avrei potuto affrontare e portare a termine questo progetto.

Un grazie va quindi ai miei genitori, Marina e Alberto, e in particolare a mia madre per avermi sempre supportata e aiutata a modo suo. Ai miei nonni, Alda e Salvatore, per essere sempre stati presenti e per non avermi mai fatto mancare nulla. A Beppe, per essere sempre riuscito a regalarmi un sorriso anche nei momenti più tristi. A Giulia e Martina, per essere cresciute al mio fianco. A Francesca, per avere condiviso con me questi cinque anni rivelatisi difficili, ma anche indimenticabili. Ad Andrea, per la vita passata, ma soprattutto per la nuova vita che ci aspetta.

Infine un immenso grazie va a Tony, per avermi insegnato che quando si cucina è sempre meglio abbondare…"si sa mai che passi qualcuno".